NASA TECHNICAL NOTE

NASA TN D-5266

C. 1

NASA TN D-5266

A PROPOSED MODEL FOR THE EFFECT OF OXIDATION ON THE HIGH-TEMPERATURE DEFORMATION OF NICKEL

by James S. Wolf
Lewis Research Center
Cleveland, Ohio

NATIONAL AERONAUTICS AND SPACE ADMINISTRATION • WASHINGTON, D. C. • JUNE 1969

A PROPOSED MODEL FOR THE EFFECT OF OXIDATION ON THE HIGH-TEMPERATURE DEFORMATION OF NICKEL

By James S. Wolf

Lewis Research Center
Cleveland, Ohio

NATIONAL AERONAUTICS AND SPACE ADMINISTRATION

For sale by the Clearinghouse for Federal Scientific and Technical Information
Springfield, Virginia 22151 – CFSTI price $3.00

ABSTRACT

The high-temperature deformation of unalloyed nickel is strongly affected by the presence of surface scale layers formed when creep tests are conducted in oxygen. Under applied stresses of 6.90 to 13.79 MN/m^2 (1000 to 2000 psi), the deformation rate of specimens at 1000° C is initially enhanced and later retarded upon their contact with oxygen gas. A phenomenological model of the transient creep process is proposed which accounts for these observations in terms of the self-pressurization and barrier qualities of the scale. A generalization of this model to other materials and to other environments is considered.

A PROPOSED MODEL FOR THE EFFECT OF OXIDATION ON THE HIGH-TEMPERATURE DEFORMATION OF NICKEL

by James S. Wolf

Lewis Research Center

SUMMARY

The deformation of unalloyed nickel at 1000° C is strongly affected by the presence of surface oxide layers formed when creep tests are conducted in oxygen. Under nominal applied stresses of 6.90 to 13.79 meganewtons per square meter, the deformation rate of creep specimens is initially enhanced and later retarded upon their contact with oxygen gas.

A model was derived describing this creep deformation behavior in terms of parameters associated with the relatively thin surface oxide scale layer. The qualities of this scale layer which affected deformation were found to be (1) its natural growth stress, or grain boundary pressure, and (2) its ability to act as a barrier to the passage of deformation shears through the specimen surface. The experimental creep data were interpreted in terms of this model by a special graphical technique based upon pairs of conjugate curves. By such analyses, a closed-form solution for the deformation of nickel in creep was obtained.

Creep deformation was also found to affect the rate of scale thickening. An enhancement of scale growth was observed to be especially associated with relatively high rates of substrate deformation.

From these observations, it is concluded that the high-temperature oxidation and deformation processes are truly coupled. A generalization of this concept to other materials and other types of high-temperature test environments is discussed.

INTRODUCTION

Structural metallic materials, when put into service at elevated temperatures, are subject to plastic deformation by applied stresses. In most applications, these materials are simultaneously exposed to conditions which promote surface scale formation.

It is therefore of primary concern to determine the effects of this duplex environment upon the behavior of materials. In pursuing the study of this problem area, it is convenient to artifically partition the macroscopic phenomena into two groupings: (1) the effect of oxidation upon deformation and (2) the effect of deformation upon oxidation. This report deals mainly with the first of these two interactions - the effect of oxidation upon deformation.

Of the total oxidation-deformation interaction research, most of the experimental effort has been directed toward the determination of the effect of surface layers on deformation processes. Much of this work, in turn, has been performed on unalloyed metals near room temperature where film thickening is strongly limited by growth kinetics. The results of these investigations, which have been summarized elsewhere (refs. 1 to 3), generally indicated (1) that foreign surface films, whether they be metallic (ref. 1), natural oxides (refs. 4 to 9), or other surface chemical compounds (refs. 2, 8, and 10), tended to inhibit those deformation processes which would have otherwise been obtained and (2) that the magnitude of the inhibition was so large that it could not be attributed to any realistic physical or mechanical properties of the surface films alone. The effect of film thickness upon substrate deformation is not clearly delineated; however, there is some indication that thicker films decrease deformation more than thin films for those cases wherein natural oxides (refs. 4, 7, and 11) or other chemical compounds (ref. 10) were formed at the substrate surface. In all cases, surface films may qualitatively be considered as barriers to the egress of dislocations from the substrate (refs. 2, 9 to 13).

At elevated temperatures (i.e., of the order of one-half the absolute melting point or more), some investigators have chosen to examine the effect of various atmospheres on the deformation of highly alloyed materials (refs. 14 to 19), primarily because of the technological importance of these materials. The results of these experiments are commensurately more difficult to interpret because of the large number of possible interactions available for operation at elevated temperature. There appear to be, at least at low stresses, several indications that oxide surface layers act as barriers to high-temperature deformation processes (refs. 1, 12, 15 to 21), a behavior which is analogous to the low-temperature observations. For the case of higher stresses, several investigators have found that the deformation processes leading to failure are actually accelerated by the presence of an oxidizing environment (refs. 14, 17, 19, and 21). Under these conditions, however, it is believed that one must also consider processes other than those associated with the formation of reaction product layers at the macroscopic external surfaces of these materials.

During elevated temperature exposure especially, and perhaps at all temperatures of technical interest, one must consider the possibility of deformations arising from sources other than the applied loads. In oxidizing environments, for example, the scaling process generates lateral growth stresses which are of sufficient magnitude to produce deformation of the substrate material (refs. 22 to 25). Literature on this subject suggests that the growth stress phenomena are quite general in nature (refs. 26 to 29), indicating that deformations from this source must be accounted for in high-temperature oxidation-deformation studies.

In order to establish a causal relation between the high-temperature oxidation and deformation processes, the oxidation-transient creep characteristics of nickel have been investigated under conditions chosen such that the oxidation kinetics are not a negligible portion of the overall process. The system nickel-nickel oxide has many attributes which recommend it for such a study; they are the following:

(1) It is the sole system for which the magnitude of the natural growth stress of the scale layer has been determined (ref. 25). This allows proper design of the experimental conditions with respect to stress levels.

(2) It is the sole system for which the linear coefficient of thermal expansion of metal and oxide are nearly identical (ref. 30). This allows metallographic interpretation of structural features relatively undisturbed by the specimen cooling operation.

(3) It is one of a limited number of systems which is considered "well behaved" insofar as its oxidation kinetics are concerned. The scale produced is a single chemical compound (NiO) which thickens almost exclusively by the unilateral diffusion of metal ions through the oxide lattice (refs. 31 to 34). Perturbations in oxidation behavior may therefore be detected with relative ease.

(4) Nickel is the base metal for several technologically useful alloys and, as a consequence, the results of this research should be applicable to more complex alloy systems.

Specimens of Nickel-201 (99.4 wt.% Ni) and Nickel-270 (99.98 wt.% Ni), having nominal thicknesses ranging from 1.6 to 3.2 millimeters, were tested in creep at 1000° C (~0.73 of the absolute melting point of Ni). The transient and steady-state rates of deformation of these materials at nominal applied stresses ranging from 6.90 to 13.79 meganewtons per square meter (MN/m^2) were determined by a special analytical procedure. The results of these analyses were incorporated into a phenomenological model which characterizes the deformation of relatively pure nickel at high temperature in inert gases and in oxygen.

SYMBOLS

$\Delta(\text{gas})$	bivalued function associated with gas type
k_x	parabolic oxidation rate constant, $\mu m/sec^{1/2}$
N	number of relaxation cycles in timing interval t_j
t	time of deformation, sec

t_i	time at end of i^{th} deformation increment, sec
t_j	time interval for N load relaxations, sec
t'	time of deformation referenced to zero at inception of oxidation, sec
x, x_t	total scale thickness, μm
x_1	thickness of outer scale layer, μm
x_2	thickness of inner scale layer, μm
α	scale barrier coefficient, $sec^{-5/6}$
α'	unit scale barrier strength, $(sec^{-1/3})(\mu m^{-1})$
β_o	Andrade creep rate constant in helium, $sec^{1/3}$
$\bar{\beta}_o$	average value of β_o, $sec^{1/3}$
β_I	effective Andrade creep rate constant with passive scale layer, $sec^{1/3}$
β_{II}	effective Andrade creep rate constant with active scale layer, $sec^{1/3}$
β_{III}	effective Andrade creep rate constant with active scale layer and preoxidation, $sec^{1/3}$
β^*	Andrade creep rate constant in oxygen, $sec^{1/3}$
$\bar{\beta}^*$	average value of β^*, $sec^{1/3}$
Γ	stress-associated creep rate constant, $m^2/(MN)(sec^{1/3})$
δ	time-independent (initial) strain
ϵ_A	Andrade or transient strain
ϵ_N	nominal total strain for N relaxation cycles
ϵ_S	steady-state strain
ϵ_T	total strain
$(\epsilon_T)_i$	total strain at end of i^{th} deformation increment
ϵ'_T	total strain referenced to zero at inception of oxidation
$\dot{\epsilon}_S$	steady-state creep rate, sec^{-1}
$(\dot{\epsilon}_S)_{cc}$	steady-state creep rate determined by conjugate curve analysis, sec^{-1}
$(\dot{\epsilon}_S)_{tan}$	steady-state creep rate determined by curve tangent method, sec^{-1}

$\dot{\epsilon}_T$	total strain rate, $\sec^{-1}$
σ_a	applied creep stress, MN/m^2
$\Delta(\sigma_a)$	bivalued function associated with applied stress level
σ_g	oxide grain boundary pressure, MN/m^2
τ	time of preoxidation treatment, sec

A PROPOSED MODEL FOR THE HIGH-TEMPERATURE DEFORMATION OF AN OXIDIZING METALLIC SPECIMEN

The phenomenological model which is to be developed in this section of the report was necessarily derived in part from experiments which will be discussed later. The chronological order of the presentation has been reversed from that which actually occurred in order to simplify the assimilation and interpretation of test results.

Deformation of an Unoxidized Metal

The development which follows is based upon an extension of the earlier work of Andrade concerning the transient creep of metals (refs. 35 to 37). To set the stage for this development, consider first the deformation of a metal under constant load at elevated temperature and with no appreciable surface oxide present.

A schematic drawing of a typical strain-time diagram is presented in figure 1. Curve 1 is usually determined in the laboratory by monitoring strain-sensing indicators and timing devices. An initial time-independent loading strain δ is normally observed, immediately followed by a decreasing rate of extension and then by the approach to a steady-state deformation rate $\dot{\epsilon}_S$. The creep behavior at still longer times, which ultimately leads to failure, will not be considered here.

If the total strain ϵ_T is sufficiently small (i.e., a few percent) as is the case assumed for this analysis, then testing at a constant applied load provides an essentially constant stress on the specimen. Under this condition, Andrade's analysis of the transient creep process is presumed to be valid and the transient deformation may therefore be described by

$$\epsilon_A = \beta_0 t^{1/3} \tag{1}$$

where ϵ_A is the Andrade (transient) creep strain, β_0 is the Andrade creep rate constant, and t is time as measured from the instant of load application. This component of the strain is represented by curve 2 in figure 1. The steady-state deformation ϵ_S is described by

$$\epsilon_S = \dot{\epsilon}_S t \tag{2}$$

where $\dot{\epsilon}_S$ is the steady-state deformation (creep) rate. This component of the deformation is represented by curve 3 of figure 1. The total strain, which is that normally observed, may thus be synthesized as the sum of the time-independent δ, steady-state ϵ_S, and transient ϵ_A strain components, that is

$$\epsilon_T = \delta + \dot{\epsilon}_S t + \beta_o t^{1/3} \tag{3}$$

It is also desirable to consider the strain rate behavior of the material being tested. This requires that extension data be determined with sufficient rapidity to allow an approximation of the instantaneous strain rate. The analytical form of the total (observed) strain rate is given by differentiation of equation (3) with respect to time; thus,

$$\dot{\epsilon}_T = \dot{\epsilon}_S + \frac{\beta_o}{3} t^{-2/3} \tag{4}$$

A schematic graph of equation (4) is shown in figure 2(a) in which the total strain rate $\dot{\epsilon}_T$ is plotted as a function of $t^{-2/3}$. The slope of this linear graph is numerically equal to one-third of the Andrade creep rate constant (i.e., $\beta_o/3$), and the intercept at infinite time ($t^{-2/3} = 0$) is the steady-state creep rate $\dot{\epsilon}_S$.

After $\dot{\epsilon}_S$ is thus determined, it is now possible to rearrange equation (3) into the following form:

$$\epsilon_T - \delta - \dot{\epsilon}_S t = \beta_o t^{1/3} \equiv \epsilon_A \tag{5}$$

and to plot the terms of the left side of this equation, the Andrade creep strain, against $t^{1/3}$ as shown schematically in figure 2(b). The slope of this linear graph is the Andrade creep rate constant β_o. Comparison of the slopes of the conjugate curves shown in figure 2 provides an internal check upon the reliability of both the experimental data and the method of analysis.

Deformation of an Oxidized Metal

Case 1: The passive surface layer. - As has been pointed out in the INTRODUCTION, one major effect of surface compound formation upon specimens subjected to an applied load is the diminution of their deformation. Microscopic analyses of this phenomenon, which is commonly termed the "barrier effect," have been presented in detail elsewhere (refs. 9, 11, and 13). The role of a passive surface oxide as a deformation barrier will now be explored in order to extend the phenomenological model described in the preceding section of this report.

Both the fact that the surface layer is less deformable than the substrate metal (e.g., NiO compared to Ni (ref. 25)) and the fact that the surface layer increases in thickness with time imply that, as testing progresses, the deformation rate of a metal-metal oxide composite under constant stress continuously diminishes. From experimental evidence to be presented in the RESULTS AND DISCUSSION, it is inferred that this is, in fact, the case. This observation will now be employed to form a first extension of the aforementioned deformation model.

If the deformation data of oxidized specimens are plotted using the format of figure 2(a), two objectionable results arise: (1) the data describe a curve rather than a straight line and (2) the intercept ε_S is negative and therefore not physically interpretable. These objections may be circumvented, and the time-dependent diminution of the deformation may be described if the Andrade rate constant β_O is reduced by a function dependent on the scale thickness x; that is, assume

$$\beta_I = \beta_O - f(x) \tag{6}$$

where β_I is the effective Andrade rate constant applicable under oxidizing conditions. For the sake of simplicity, assume further that the following first-order approximation is valid:

$$f(x) = \alpha' x \tag{7}$$

where α' is a constant. Within the limits of this approximation, it may also be presumed that the scale thickens in a parabolic fashion (ref. 33); thus,

$$x = k_x t^{1/2} \tag{8}$$

where k_x is the parabolic rate constant based upon scale thickening. Equations (6), (7), and (8) may be combined to yield the following expression for β_I:

$$\beta_I = \beta_O - \alpha t^{1/2} \tag{9}$$

where α, which is defined as $\alpha' k_x$, may be stress dependent.

Under the combined conditions of oxidation and deformation, the rate constant β_o of equation (3) is replaced by the effective rate constant β_I of equation (9) to give the total strain as

$$\epsilon_T = \delta + \beta_o t^{1/3} - \alpha t^{5/6} + \dot{\epsilon}_S t \tag{10}$$

Note that this equation holds only if the oxidation and deformation processes are initiated simultaneously. It follows that the total strain rate is given by

$$\dot{\epsilon}_T = \frac{\beta_o}{3} t^{-2/3} - \frac{5\alpha}{6} t^{-1/6} + \dot{\epsilon}_S \tag{11}$$

Equations (10) and (11) contain three undetermined parameters: β_o, α, and $\dot{\epsilon}_S$. In order to facilitate a graphical solution of these equations, it may be assumed that $\dot{\epsilon}_S$ is negligibly small.[1] For this case, equations (10) and (11) become

$$\epsilon_T - \delta + \alpha t^{5/6} = \beta_o t^{1/3} \tag{12}$$

and

$$\dot{\epsilon}_T + \frac{5\alpha}{6} t^{-1/6} = \frac{\beta_o}{3} t^{-2/3} \tag{13}$$

By using equation (13), the constant α may be approximated from the total strain-rate data by an iteration process which involves plotting the left side of equation (13) against $t^{-2/3}$, and simultaneously demanding a linear graph which passes through the origin. As in figure 2(a), the slope of this graph is one-third of the unmodified Andrade rate constant; that is, $\beta_o/3$. Similarly, the left side of equation (12), when plotted against $t^{1/3}$, must again yield a linear graph with slope β_o. Comparison of the slopes and the approach of the data to linearity in the conjugate plots of equations (12) and (13) provides an internal check of the parameters α and β_o and of the assumption that $\dot{\epsilon}_S$ approaches zero as the time of testing becomes infinite.

Case 2: The active surface layer. - Equations (12) and (13) describe the deformation of a metallic specimen covered with a thickening, but otherwise passive surface scale layer. It has been found, however, that a growing oxide, and more particularly nickel oxide growing upon nickel, is not passive in that a lateral compressive stress is generated in the scale during the oxidation process (ref. 25). This stress, which has

---

[1] It will be demonstrated later that $\dot{\epsilon}_S$ tends toward zero as the time of oxidation increases.

been termed grain boundary pressure, will be hereafter denoted by σ_g. For the case of nickel oxide growing upon nickel in oxygen at 1000° C, the mean value of σ_g has been found to be approximately 10 MN/m^2 (ref. 25).

The immediate effect of a compressively stressed oxide surface layer upon substrate deformation may be seen with the aid of the schematic diagram shown in figure 3. It is assumed for the sake of discussion that some stress-free initial scale layer exists early in the oxidation process (fig. 3(a)). As the scale is allowed to thicken by a hypothetical process wherein the substrate donates material to the scale for further growth, but is not constrained to it at the metal-oxide interface, a lateral growth of the scale layer would be noted (fig. 3(b)). This lateral growth is believed to be associated with the deposition of a small amount of new oxide at preexisting columnar grain boundary sites in the scale (ref. 25). Finally, upon reapplication of the constraint at the metal-oxide interface (fig. 3(c)), it is seen that a compressive stress is developed in the scale layer and that a complimentary tensile stress is obtained in the substrate. For sufficiently thin metal substrates, this stress distribution leads to overall material elongation as shown in figure 3(c) (ref. 25). The presence of a compressively stressed oxide surface layer on a metal in tension at low applied stresses will tend to aid those processes which promote specimen elongation. This is in direct opposition to the effect of the barrier-like properties (with respect to dislocation egress) which the same scale exhibits because of its presence on the specimen surface.

Because σ_g is believed to arise from a chemical reaction at the oxide grain boundary network, it will be assumed that the oxide growth process tends to maintain some (thermodynamically) fixed value of this compressive stress. This assumption for the growing scale is adopted in analogy to the observation that crystals growing from aqueous solution appear to exhibit an equilibrium crystal pressure (ref. 29). In both cases, a new phase is produced and is grown from its surroundings in a directed manner to produce the crystal (or grain boundary) pressure.

A very simplified approach will be used to incorporate the concept of scale self-pressurization into the deformation equations. It will be assumed that, at tensile stresses of magnitude less than that of σ_g, the oxide will tend to expand laterally in the direction of the applied stress and thus aid deformation. Conversely, at tensile stresses greater in magnitude than that of σ_g, the scale will tend to contract, in order to maintain its pressure, and thus will tend to inhibit deformation. In addition, the degree of aid or inhibition provided by the scale to the deformation process will be presumed to be linearly related to the difference between the applied stress and σ_g. These thoughts may be expressed in analytical form by an alteration of the creep rate constant such that

$$\beta_{II} = \beta_o + \Gamma(\sigma_g - \sigma_a) - \alpha t^{1/2} \tag{14}$$

where β_{II} is the effective Andrade creep rate constant, Γ is a stress-associated deformation rate constant, and σ_a is the applied tensile stress.

The effective Andrade rate constant for transient creep β_{II} is thus composed of three terms: (1) β_o which may be envisioned as an intrinsic rate constant and which is the sole term in the case that no scale layer forms, (2) the term $\Gamma(\sigma_g - \sigma_a)$ which accelerates the deformation process at low stresses and retards it at high stresses and which arises from self-pressurization of the scale layer, and (3) the term $\alpha t^{1/2}$ which retards deformation at all stresses because the scale acts as a barrier to the passage of deformation shears.

It follows from equations (3) and (14) that the total strain is given by

$$\epsilon_T = \delta + \left[\beta_o + \Gamma(\sigma_g - \sigma_a)\right]t^{1/3} - \alpha t^{5/6} + \mathring{\epsilon}_S t \tag{15}$$

and that the total strain rate is therefore given by the following expression:

$$\mathring{\epsilon}_T = \frac{\left[\beta_o + \Gamma(\sigma_g - \sigma_a)\right]}{3} t^{-2/3} - \frac{5\alpha}{6} t^{-1/6} + \mathring{\epsilon}_S \tag{16}$$

It will now prove convenient to define a rate constant β^* such that

$$\beta^* = \beta_o + \Gamma(\sigma_g - \sigma_a) \tag{17}$$

to again impose the condition that $\mathring{\epsilon}_S$ is negligibly small and to rearrange equations (15) and (16) into the following forms:

$$\epsilon_T - \delta + \alpha t^{5/6} = \beta^* t^{1/3} \tag{18}$$

and

$$\mathring{\epsilon}_T + \frac{5\alpha}{6} t^{-1/6} = \frac{\beta^*}{3} t^{-2/3} \tag{19}$$

When the applied tensile stress is equal in magnitude to the grain boundary pressure (i.e., $\sigma_a = \sigma_g$), equations (18) and (19) reduce to equations (12) and (13), respectively, which describe the deformation for the case of a passive surface layer. However, at any other applied stress, the effect of self-pressurization of the scale layer enters into the deformation behavior. For all stress levels equations (18) and (19) may be plotted using the general format of the conjugate diagrams shown in figure 2 with the exceptions (1) that the slopes of the linear graphs will now be $\beta^*/3$ and β^* rather than $\beta_o/3$ and

β_o and (2) that the ordinates will now be Andrade strain rates and strains corrected for the barrier effect (i.e., corrected by terms containing α).

The values of the parameters σ_g and Γ may be determined from a prior knowledge of β_o and β^* by a graphical technique based on equation (17). This equation may be rearranged to form

$$\beta^* - \beta_o = \Gamma(\sigma_g - \sigma_a) \tag{20}$$

If deformation data are available at several levels of applied stress, then, by an iterative choice of σ_g, a linear graph of $\beta^* - \beta_o$ against $\sigma_g - \sigma_a$ may be developed which passes through the origin and which has slope Γ.

Case 3: The oxide layer formed prior to deformation. - In those instances where the specimen has been oxidized for some time τ prior to the initiation of deformation, the value of β_{II} must be adjusted commensurately. Under this condition, equation (14) becomes

$$\beta_{III} = \beta_o + \Gamma(\sigma_g - \sigma_a) - \alpha(\tau + t)^{1/2} \tag{21}$$

where β_{III} is the effective Andrade rate constant applicable to this case, the time τ is measured from the instant of initiation of oxidation to the instant of initiation of load application, and the time t is measured from the instant of initiation of load application. Thus, from equations (3) and (21), the total deformation may be expressed as

$$\epsilon_T = \beta^* t^{1/3} - \alpha(\tau + t)^{1/2} t^{1/3} + \dot{\epsilon}_S t + \delta \tag{22}$$

and the total strain rate as the first time derivative of this quantity

$$\dot{\epsilon}_T = \frac{\beta^*}{3} t^{-2/3} - \frac{\alpha}{3} (\tau + t)^{1/2} t^{-2/3} - \frac{\alpha}{2} (\tau + t)^{-1/2} t^{1/3} + \dot{\epsilon}_S \tag{23}$$

Rearrangement of these equations gives

$$\epsilon_T - \delta + \alpha(\tau + t)^{1/2} t^{1/3} - \dot{\epsilon}_S t = \beta^* t^{1/3} \tag{24}$$

and

$$\dot{\epsilon}_T + \frac{\alpha}{3} (\tau + t)^{1/2} t^{-2/3} + \frac{\alpha}{2} (\tau + t)^{-1/2} t^{1/3} = \frac{\beta^*}{3} t^{-2/3} + \dot{\epsilon}_S \tag{25}$$

Equations (24) and (25) reduce to equations (18) and (19), respectively, for the case of the active surface layer if the value of τ is zero. As before, they may be plotted using the general format of the conjugate curves shown in figure 2, provided that the values of τ and α are known and with the exceptions (1) that the slopes of the linear graphs will now be $\beta^*/3$ and β^* rather than $\beta_0/3$ and β_0 and (2) that the ordinates will now be Andrade strain rates and strains corrected for the effect of preoxidation by the terms containing α and τ.

EXPERIMENTAL PROCEDURE

Materials

Two grades of nickel were employed during the course of this investigation. One grade, Nickel-201, contained approximately 99.4 weight percent nickel and was susceptible to internal oxidation by virtue of its residual impurities. The other grade, Nickel-270, was nominally 99.98 weight percent nickel. The nominal compositions of these materials is given in table I. Both materials were received in the form of hot-rolled sheet approximately 3.2 millimeters in thickness. A portion of the Nickel-201 sheet was further reduced in thickness for use in special experiments by conventional cold-rolling.

Specimen Preparation

Test specimens of the configuration shown in figure 4 were machined from the sheet material such that the longest dimension (tensile axis) was oriented parallel to the rolling direction. Subsequent to surface machining and inspection, each specimen was metallographically polished by hand through 3-micron diamond abrasive. The specimens were then electropolished over their entire gage length using the conditions listed in table II. Material removal resulting from this operation was approximately 0.01 millimeter from each of the exposed surfaces and thus provided surfaces free of residual cold work. The wedge-shaped specimen ends were protected during electropolishing by use of a "stop-off" lacquer.

Rectangular companion specimens, used for control purposes, were machined from the same small lots of material as were the test specimens. These specimens were cut into pieces approximately 19 millimeters long by 13 millimeters wide with the longer dimension parallel to the rolling direction of the sheet. Mechanical and electrolytic polishing operations were performed on these specimens in a manner identical to that employed for the creep test specimens.

After electropolishing, both types of specimens were inspected for surface defects, thoroughly cleaned with acetone and methyl alcohol, and stored in glass vials until placed in the test apparatus. Specimens were held in the test chamber with flat Inconel grips which were machined at one end to accept the wedge-shaped portion of the specimens and were bored at the other end to accept a round pin which fastened them to the test chamber ends.

Constant Load Creep Tests

The first series of tests, involving only those specimens fabricated of Nickel-201, were performed in a gas-tight furnace mounted on a 10-to-1 ratio constant load creep machine. This apparatus with its auxiliary equipment is shown schematically in figure 5. The primary purpose of this series of tests was to determine the effect of oxidation at 1000° C upon the deformation characteristics of nickel for the stress range from approximately 6.90 to 13.79 MN/m^2.

Prior to testing, the apparatus was carefully leveled and balanced in a manner which took into account the mass of the upper bellows and the associated specimen support system. The test and control specimens as well as a platinum - 13 percent rhodium-platinum sensing thermocouple were centrally mounted in the hot zone of the test chamber. The thermocouple and the control specimen were mounted on opposite sides of the tensile creep specimen and were separated from it by approximately 5 millimeters distance. The test chamber was then purged for approximately 10^5 seconds with helium which had been passed through a molecular sieve and an acetone-dry ice cold trap to ensure its freedom from oxygen and water vapor. Only after these conditions were fulfilled was the furnace heated to the test temperature. The specimen was subjected to a minor tensile load (less than 2 MN/m^2) during the heating operation. A constant pressure head of helium was maintained within the furnace chamber throughout these tests by forcing the gas through a bubbler bottle, filled to a depth of 10 millimeters with dibutylphthylate, at the rate of 1 to 2 cubic centimeters per second.

Subsequent to thermal stabilization, the test load was applied and the specimen extension in helium at 1000° C was monitored by means of a sensitive dial indicator. These test conditions were maintained until the rate of deformation $\dot{\varepsilon}_T$ approached a nearly constant value at which time oxygen was admitted to the test chamber through the cold trap by means of a manifold valve. The helium flow was simultaneously stopped, and the oxygen flow rate was set at 1 to 2 cubic centimeters per second. Deformation was monitored as a function of time for the ensuing period ($\sim 1.5 \times 10^4$ sec) after which the test was terminated.

The strain-time diagrams, similar to that shown schematically in figure 1, were established using tabulated values of extensions and corresponding times. Strain rates were determined by a difference method in which the strain increment was divided by the time interval for an adjacent pair of strain-time points. This method of analysis is outlined schematically in table III. Just as the strain $(\epsilon_T)_i$ was associated with the time t_i, so was the strain rate $\left[(\epsilon_T)_{i+1} - (\epsilon_T)_i\right]/(t_{i+1} - t_i) = \dot{\epsilon}_T$ associated with the average time $t_i + \left[(t_{i+1} - t_i)/2\right]$.

Stress-Relaxation Creep Tests

The purpose of this second series of tests was to complete the survey of the effect of oxidation upon deformation and to investigate the effect of deformation upon oxidation, especially with regard to the purer grade of nickel. Specimens were fabricated of both Nickel-201 and Nickel-270 and were tested using a stress-relaxation method for the determination of deformation rates. All tests were performed at 1000° C and all but one at a nominal stress level of 6.90 $\mathrm{MN/m^2}$.

A screw-driven testing machine, fitted with a load-sensing device and supporting the same furnace chamber described previously, was used in these experiments. The test chamber was modified in that a thin Nickel-201 sleeve was fitted to the internal diameter of the furnace core. This modification minimized the transfer of chromium or other deleterious elements which could adversely affect interpretation of the oxidation process from the relatively hot stainless-steel chamber wall to the specimens. The deformation of specimens is relatively insensitive to the presence (or absence) of this modification.

Specimen configuration and preparation, as well as furnace startup procedure, were identical to that described previously. After attaining thermal equilibrium with the minor tensile load applied, the major tensile load was attained by driving the machine crosshead until a predetermined load (stress) indication was obtained. The load was then allowed to relax by the natural creep processes until a lower load limit (~3 percent decrement) was reached; the load was then increased (3 percent) by crosshead drive to the maximum load value, and so forth. Cam-operated microswitches of a load controller allowed this sequence to repeat itself in a fully automatic fashion.

A determination of the number of relaxations per unit time provided a proportional measure of the instantaneous creep rate. The constant of proportionality was estimated by determining the average crosshead displacement per relaxation cycle with a dial micrometer.

A schematic relaxation test output is shown in figure 6, and associated calculations are outlined in table IV. Just as the total strain $(j)(\epsilon_N)$ is associated with the elapsed time $\sum_{1}^{i} t_j$, so is the total strain rate ϵ_N/t_{j+1} associated with the average time

$\sum_{1}^{i} t_j + (t_{j+1}/2)$. The cycle increment N was arbitrarily chosen to have the value 10, and the nominal strain increments ϵ_N were therefore essentially constant.

The procedure for the series of stress-relaxation tests was varied from that for the constant load tests so the effect of various preoxidation times upon deformation behavior could be studied.

Metallographic Examination

The structural character of both the deformed (creep) and undeformed (control) specimens was examined metallographically after testing. Each specimen was sectioned normal to the original rolling direction using a fine-toothed jeweler's saw, mounted in a thermosetting plastic, and polished to provide a metallographic section normal to the rolling direction. Subsequent to the chemical and electrolytic etching described in table V, photomicrographs of the cross sections were made and the scale thicknesses of oxidized specimens were determined.

The thickness of each scale layer as well as the total scale thickness was determined for five selected specimen pairs of Nickel-270. From such measurements, at 10 equally spaced intervals along both of the two longer section dimensions, values for the average thickness of the outer scale layer x_1, the inner scale layer x_2, and the total scale layer x_t were determined. A comparison of these average values for each specimen pair was then made in order to determine the effect of creep deformation upon oxide scale thickening.

The system employed for measuring scale thicknesses utilized a filar eyepiece mounted on the monocular body of a research metallograph. This optical system was calibrated with a metric stage micrometer. Most of the oxide scales were measured with a precision such that one unit of the filar eyepiece screw (the least count of the optical system) was equal to 0.0913(2) micrometer. For two instances wherein the scale layer was relatively thin, the magnification was increased such that one filar eyepiece unit equalled 0.0701(3) micrometer. The reproducibility of a given measurement was found to be within 2 filar units, or approximately ±0.2 micrometer.

RESULTS AND DISCUSSION

In the discussion which follows, all results are interpreted in terms of one of three cases presented in the proposed model. Test results obtained in helium or argon atmospheres are analyzed on the basis of the section Deformation of an Unoxidized Metal. Test results obtained in an oxygen atmosphere are analyzed on the basis of the section

Deformation of an Oxidized Metal. Data obtained without preoxidation are analyzed under case 2, and that with preoxidation are analyzed under case 3.

Constant Load Creep Tests

Strain-time behavior. - Strain-time curves derived from constant load tests at 1000° C are shown in figure 7. The total strain, less the initial time-independent deformation δ, is plotted against time at load for nominal applied stress levels of 6.90, 10.34, and 13.79 MN/m^2 acting on specimens of Nickel-201. Each set of data exhibits a deformation increment (and a deformation rate increment) just subsequent to the time of oxygen admission into the test chamber. Inspection of figure 8 reveals that this effect is less pronounced as the magnitude of the stress is increased. This observation qualitatively substantiates equation (14). The strong similarity between the curves shown in figures 7(a) and (b) indicates that the magnitude of the rate increment is not dependent upon specimen thickness (therefore, it is also independent of specimen surface-to-volume ratio) and infers that a surface rather than bulk phenomenon is involved as had been assumed previously.[2]

The magnitude of the strain increment observed at an applied stress of 6.90 MN/m^2 relative to the deformation behavior of virgin material tested at 6.90 and 10.34 MN/m^2 is illustrated in figure 9. The solid curve represents the data of figure 7(a). At the time that the strain increment was initiated, a new coordinate system (ϵ_T' against t') was superimposed as shown. The deformation curves established in helium at 6.90 and 10.34 MN/m^2 (figs. 7(a) and (c)) were then plotted in the new coordinate system. From this construction, it may be seen that the deformation behavior in oxygen at 6.90 MN/m^2 is initially intermediate to that of previously unstrained material tested at the stress levels of 6.90 and 10.34 MN/m^2. At longer times, the deformation produced in the oxidizing specimen is less than that produced in the helium-tested specimen subjected to the same applied stress, 6.90 MN/m^2. This overall behavior suggests that two counteracting effects exist in the oxidizing specimen, one aiding deformation and the second hindering deformation. It is for this reason that the σ_g and α terms, respectively, were introduced in the preceding section.

---

[2] The possibility that a transient temperature increment was generated because of the admission of oxygen and that this was, in turn, responsible for the observed deformation increments was negated by a separate experiment in which no temperature change could be detected when a thin coupon of nickel was monitored continuously. A thermocouple spot-welded to the coupon was used to determine that a temperature change of less than 1/2° C was induced during the cycle in which the surrounding gas was changed from helium to oxygen.

Conjugate curve analysis. - The deformation data for tests in helium, represented by the initial portions of the curves in figure 7, were analyzed using the conjugate curve technique outlined previously and are shown in figures 10 and 11. These curves are based on equations (4) and (5), respectively, and are plotted using the format shown schematically in figure 2.

It is seen that both the strain rate data (fig. 10) and the strain data (fig. 11) are well represented by their respective linear graphs. Further, the Andrade creep rate constants β_o agree to within less than 2 percent for each conjugate set of data representing the four specimens tested. The slightly larger scatter noted in the strain rate data is to be expected on the basis of the mode of data collection employed. This scatter is essentially integrated out (on a time basis) to give the good fit to the linear graphs shown in figure 11.[3]

The deformation data for the same specimens tested in an oxidizing atmosphere, represented by the final portions of the curves shown in figure 7, were similarly analyzed by the conjugate curve technique. In this analysis, however, the primed strain-time coordinate system of reference suggested by figure 9 was employed. The results of this analysis are presented in figures 12 and 13, which are, in turn, based upon equations (18) and (19), and are plotted using a commensurate modification of the format shown schematically in figure 2.

As in the case of the helium atmosphere tests, both the strain rate data and the strain data are well represented by their respective linear graphs. In each case, the value of the barrier coefficient α was chosen by an iteration process (to within ±20 percent) such that (1) the curves representing the data were linear, (2) the curves passed through the origin, and (3) the value of the creep rate constants β^* were nearly equal for each conjugate set of curves. The creep rate constants were found to agree with one another to within less than 6 percent for each set of conjugate data.

Interpretation of deformation data. - The purpose of this section of the report is to summarize and interpret the results of the conjugate curve analyses in terms of the deformation model presented earlier. Values of the parameters $\mathring{\varepsilon}_S$, β_o, β^*, and α have been collected and are presented in table VI. From these data it is seen that, as the stress is increased, in a given gaseous environment, the values of both the steady-state and the transient creep rate constants increase, as expected. The relative average values of the Andrade creep rate constants $\bar{\beta}_o$ and $\bar{\beta}^*$ change with the absolute value of the applied stress in qualitative agreement with equation (17). Thus, at low stresses, the Andrade creep rate constant is larger in an oxygen environment; whereas, at high stresses, it is larger in a helium environment. The values of the barrier coefficient α

---

[3] Deviations from linearity are most pronounced during initial test stages because of initial transients. Similar effects are described later in the section on stress-relaxation tests.

at the lower stresses were found to be approximately five times larger than that which applies at the highest stress. This change in α suggests that the deformation process changes in character as the applied stress is increased beyond some critical limiting value.

It is inferred that this critical stress is the same as that which was postulated to affect the rate of transient deformation; that is, the critical stress is that associated with the grain boundary pressure of the growing surface oxide scale. The numerical value of the grain boundary pressure σ_g may be evaluated on the basis of equation (20). The average values of the Andrade creep rate constants $\bar{\beta}_o$ and $\bar{\beta}^*$ as given in table VI were used to construct the graph of figure 14. By an iterative method, the value of σ_g was determined to be 10.59 MN/m^2 which agrees well with the approximate value of 10.3 MN/m^2 as determined earlier by a totally different technique (ref. 25). The slope of the graph shown in figure 14 provides the value of the stress-associated rate constant Γ which is 3.40×10^{-4} $m^2/(MN)(sec^{1/3})$, while the fit of the data to this linear graph substantiates the validity of equation (20) of the model.

Finally, the effective Andrade rate constant β_{II} may now be calculated as a function of the time of deformation t since the parameters Γ, σ_g, and α are known. Equation (14) was recast to the following form:

$$\frac{\beta_{II}}{\bar{\beta}_o} = 1 + \frac{\Gamma}{\bar{\beta}_o} (\sigma_g - \sigma_a) - \frac{\alpha}{\bar{\beta}_o} t^{1/2} \qquad (26)$$

and the ratio $\beta_{II}/\bar{\beta}_o$ was calculated as a function of time using the parameters listed in table VI. The results, presented in figure 15, express the instantaneous values of the effective Andrade rate constants under oxidizing conditions with respect to those (time-independent) values determined from tests in helium.

The value of this ratio decreases monotonically with time at all stresses, but with varying degree as dictated by the particular scale barrier coefficient α. At the lowest stress and for times corresponding to those investigated, the ratio always exceeds unity. This behavior emphasizes the observation that at low stresses the transient creep is of larger magnitude in oxygen than it is in helium which, in turn, is inferred to be primarily due to the dominant effect of grain boundary pressurization at low stresses. At the intermediate stress, the ratio is first greater than unity and subsequently less than unity. This is interpreted in terms of an initial predominance of the grain boundary pressurization effect and a later predominance of the scale layer barrier effect to provide a long-term rate constant smaller than that associated with deformation in helium. At the highest stress investigated, both the scale pressurization and scale barrier effects act in concert to provide ratios of creep rate constants $\beta_{II}/\bar{\beta}_o$ that are less than unity throughout the period of testing.

Stress-Relaxation Creep Tests of Nickel-201

Strain-time behavior. - Three tests were performed with specimens of Nickel-201, nominally 3.2 millimeters thick, using the stress-relaxation testing technique described in the EXPERIMENTAL PROCEDURE section. The purpose of these tests was to determine the effect of oxidation prior to deformation (or preoxidation) upon the subsequent deformation of this material and to thereby test the validity of the final portion (Case 3) of the proposed deformation model. These tests, which were conducted at 1000° C and an applied stress of 6.90 MN/m^2, involved (1) zero preoxidation time and deformation in helium, (2) 1.44×10^4 seconds preoxidation in oxygen with subsequent deformation in oxygen, and (3) 5.76×10^4 seconds preoxidation in oxygen with subsequent deformation in oxygen.

The resulting strain-time curves, determined as outlined in table IV, are presented in figure 16. It is seen that, as the preoxidation time τ is increased, the total strain at any later time of deformation t is decreased. This observation is in qualitative agreement with equation (22) of the model and reflects the effect of the scale barrier coefficient α.

Conjugate curve analysis. - The deformation data illustrated in figure 16 were also analyzed by the conjugate curve technique. The results of this analysis are shown in the strain rate-time and strain-time curves of figures 17 and 18. For the single test run in helium, equations (4) and (5) were employed in the analysis; whereas, because preoxidation is involved, the tests run in oxygen were analyzed using equations (24) and (25). The application of these latter equations requires a prior knowledge of the scale barrier coefficient α in addition to those quantities determined by direct observation or elementary calculation. From an examination of table VI, the value 0.60×10^{-5} $\text{second}^{-5/6}$ for α was selected as being suitably representative for the purpose of this analysis.

It is seen that both the strain rate data (fig. 17) and the strain data (fig. 18) are well represented by their respective linear graphs. Further, the creep rate constants β_o and β^* agree to within less than 1 percent for each conjugate set of data representing the three specimens tested. Because the strain rate data is determined by a more direct means in the stress-relaxation-type test, the strain rate data of figure 17 exhibit less scatter than those obtained by the analysis of constant load creep data (fig. 10).

Interpretation of deformation data. - The purpose of this section of the report is to summarize and interpret the data of figures 16 to 18 in terms of the deformation model. Values of the parameters $\mathring{\epsilon}_S$, β_o, and β^* have been collected and are presented in table VII.

The average value of the Andrade creep rate constant $\overline{\beta}_o$ for the specimen tested in helium was found to be 5.16×10^{-4} $\text{second}^{-1/3}$. This value is lower than that determined under similar conditions by the constant load creep technique ($\overline{\beta}_o = 8.05\times10^{-4}$ $\text{sec}^{-1/3}$). Although the testing methods differ, it is believed that the discrepancy in the value of the creep rate constant most probably arises by virtue of the fact that the absolute value of the strain per relaxation cycle is not known with certainty. This, however, in no way detracts from the worth of the relative values of strain and strain rate as determined by the relaxation technique; that is, specimen-to-specimen comparisons are believed to be valid within that group of specimens tested by the stress-relaxation technique. For example, the observation that β^* is larger than β_0 at the applied stress of 6.90 MN/m^2 (see table VII) is in qualitative agreement with both the model and the constant load creep test results.

In analogy with the analysis of the constant load creep test data, the ratio of the creep rate constants $\beta_{III}/\bar{\beta}_0$ was determined for the stress-relaxation tests. Equations (17) and (21) were combined and rearranged to give

$$\frac{\beta_{III}}{\bar{\beta}_0} = \frac{\beta^*}{\bar{\beta}_0} - \frac{\alpha}{\bar{\beta}_0} (\tau + t)^{1/2} \tag{27}$$

from which this ratio was calculated as a function of the time of deformation t using the values of the parameters listed in table VII. The results of this calculation, presented in figure 19, express the instantaneous values of the effective Andrade rate constant under oxidizing conditions and as a function of the preoxidation time τ relative to that value of the rate constant determined from the stress-relaxation test performed in helium. The upper curve of figure 15 which was derived from the constant load tests is transposed to figure 19 for the purpose of ready comparison.[4]

Figure 19 shows that, as the preoxidation time τ is increased, the rate constant ratios are reduced by a factor of 5 or more with respect to the ratio for the specimen with no preoxidation. This tendency for preoxidation to strongly attenuate transient creep is interpreted on the basis that the scale barrier is dominant in regulating the transient deformation process - especially for the case of the relatively long preoxidation times involved. Further, thicker oxide scale layers appear to be better barriers to deformation than do thin layers, which is in qualitative agreement with the proposed model. A quantitative check of this statement may be made through the use of equation (27) by plotting the values of $\beta_{III}/\bar{\beta}_0$ (for the testing time $t = 0$) against the square

---

[4] This comparison is believed to be valid because: (1) the effective rate constant β_{III} reduces to the constant β_{II} when the preoxidation time is zero (see eqs. (14) and (21)); (2) the specimens were tested at the same level of applied stress and temperature; (3) the specimens are of the same nominal thickness; and (4) any factorial error in absolute strain measurement would be eliminated through the calculation of the creep rate constant ratios.

root of the preoxidation time τ. This was done in figure 20, and a line through the data was established by fixing the intercept to be the average value of $\overline{\beta^*/\beta_0}$ and by fixing the slope to be the average value of $-\overline{\alpha/\beta_0}$ for the three specimens in question. It is seen that the extreme data points fit the straight line rather well; however, the central data point, representing the specimen preoxidized for 1.44×10^4 seconds, exhibits a strong negative deviation from the line.

The deviation from the projected value of β_{III}/β_0 arises because the Andrade rate constant in oxygen β^* for this specimen is smaller than that predicted on the basis of the deformation model. Equation (17), coupled with the previously determined values of β_I and σ_g, was used to calculate the model value of β^* as 17.7×10^{-4} $\text{second}^{-1/3}$. This is approximately 50 percent larger than that value determined for the specimen preoxidized for 1.44×10^4 seconds, while it is approached (within 15 percent) by the value determined for the specimen preoxidized for 5.76×10^4 seconds.

Finally, some inferences concerning the effect of preoxidation upon deformation may be drawn from an examination of the steady-state creep rates. For this purpose, the steady-state creep rate constants $\dot{\varepsilon}_S$, evaluated both by the conjugate curve analysis and from the terminal tangents of the curves of figure 16, are collected and presented in table VII. It is seen that the tangent values of $\dot{\varepsilon}_S$ are always larger than or equal to those values determined by the conjugate curve technique, indicating that some significant degree of transient creep remains.[5] However, both sets of rate values indicate that the apparent steady-state deformation is decreased by a factor of 3 to 5 as the preoxidation time is increased from 1.44×10^4 to 5.76×10^4 seconds. Further, the tabulated ratios of the conjugate curve values divided by the tangent values $\left(\dot{\varepsilon}_S\right)_{cc}/\left(\dot{\varepsilon}_S\right)_{tan}$ indicate that increasing amounts of preoxidation reduce the proportion of transient creep contributing to the total deformation. This conclusion is in qualitative agreement with the results presented in figure 19. Both of these observations, pertaining to the reduction in the steady-state and transient deformation rates with increasing amounts of preoxidation, are interpreted in terms of the scale layer acting as a barrier to deformation.

Stress-Relaxation Creep Tests of Nickel-270

Strain-time behavior. - Seven tests were performed with 3.2-millimeter-thick specimens of Nickel-270 at 1000° C using the stress-relaxation testing technique. The purposes of these tests were (1) to determine the deformation behavior of this material

---

[5] If the transient creep were to be of negligible magnitude, then the tangent value of the steady-state creep rate would exactly equal that determined by the conjugate curve technique and the rate ratio would equal unity.

both with and without preoxidation and (2) to determine the effect of deformation upon the scale thickening process.

The initial portions of the strain-time curves obtained from these tests, determined as outlined in table IV, are presented in figure 21. The curves of figure 21(a) were all obtained at a nominal applied stress of 6.90 MN/m^2. Results for the three inert atmosphere tests, two run in argon and one run in helium, are represented by the band in the upper portion of this figure. The width of this band indicates the degree of reproducibility of data from test to test.

Of the remaining curves, two represent the effect of preoxidation on the subsequent deformation behavior. Curves 1 and 3 are drawn for specimens which were oxidized 1.44×10^4 and 5.76×10^4 seconds, respectively, prior to deformation in oxygen. It is seen that increasing the time of preoxidation tends to diminish both the strain and the strain rate for all testing times. This behavior parallels that found for Nickel-201 (see fig. 16), and is in qualitative agreement with the proposed deformation model.

Curve 2 of figure 21(a) represents the data for a specimen which was instantaneously stressed to a level of approximately 7.75 MN/m^2 just prior to deformation in helium at a stress of 6.90 MN/m^2. Although the degree of overstressing was small (~12 percent), its effect is both large and persistent, with subsequent deformations reduced by approximately 30 percent. This observation suggests that any source of overstressing, and especially that associated with the deformation of metallic surface layers resulting from the self-pressurization of the adjacent oxide scale, will increase the material's resistance to further deformation.

Finally, the initial portion of the strain-time curve for the single specimen tested at the applied stress of 10.34 MN/m^2 is shown in figure 21(b). The data represent deformations observed initially in helium and later after admission of oxygen to the test chamber. As in the case for Nickel-201 (see fig. 7), strain and strain rate increments were observed indicating that the presence of oxygen initially accelerated the deformation process. Other Nickel-270 stress-relaxation specimens subjected to this duplex gas environment exhibited a similar behavior.[6]

Conjugate curve analysis. - The deformation data represented in figure 21 were also analyzed by the conjugate curve technique. The results of these analyses are shown in the strain rate-time and strain-time curves of figures 22 and 23, respectively. The three base-line tests in inert atmospheres represented by the band in figure 21(b) are analyzed in detail in figures 22(a) to (c) and 23(a) to (c). For the five tests initiated in an inert atmosphere, equations (4) and (5) were employed in the analysis; whereas,

---

[6] The increments found in these cases were not treated quantitatively because the tangent modulus of nickel, upon which the stress-relaxation technique is based, decreases rapidly after some initial testing period.

because preoxidation is involved, the two tests initiated in oxygen were analyzed using equations (24) and (25).

The application of these latter equations requires a prior knowledge of the numerical value of the scale barrier coefficient α for this material in addition to those quantities determined by direct observation or elementary calculation. Two considerations were employed to set bounding values on α: (1) from the curves of figure 21(a), it is clear that this value must be greater than zero and (2) because Nickel-270 forms only an external scale, as opposed to both the external and internal oxidation of Nickel-201, it is believed that the value must be less than or equal to that determined from the analysis of the Nickel-201 data (i.e., $0 \leq \alpha \leq 0.60\times10^{-5}$ $\text{sec}^{-5/6}$). When the data for the specimen preoxidized the longer time ($\tau = 5.76\times10^4$ sec) was used, it was found by iteration that the upper bound of α best described the deformation data.

It is seen that both the strain rate data (fig. 22) and the strain data (fig. 23) are well represented by their respective linear graphs. Further, the creep rate constants β_0 or β^* agree to within less than 3 percent for each conjugate set of data representing the seven specimens tested. For the three tests initiated in inert gas, and wherein specimens were simply stressed to 6.90 MN/m^2, the test-to-test variations in the mean values of β_0 with respect to their average are less than $7\frac{1}{2}$ percent indicating that the degree of reproducibility is satisfactory in the relaxation-type test.

Interpretation of deformation data. - The purpose of this section of the report is to summarize and interpret the data represented by figures 21 to 23 in terms of the proposed deformation model and to compare these data with those obtained from the tests of Nickel-201. Values of the parameters $\dot{\varepsilon}_S$, β_0, and β^* for Nickel-270 have been collected and are presented in table VIII.

Comparison of these values for Nickel-270 with those of Nickel-201 obtained by constant load and stress-relaxation creep testing (tables VI and VII, respectively) indicate the following:

(1) The Andrade creep rate constant in helium β_0 is larger for Nickel-270 than for Nickel-201 at the applied stress levels of both 6.90 and 10.34 MN/m^2. From this observation it is inferred that solid-solution hardening, associated with the less pure Nickel-201, is effective in reducing the transient creep rate.

(2) The Andrade creep rate constant in oxygen β^* as determined after the longer preoxidation time (5.76×10^4 sec) is equal, within experimental error, for both grades of nickel. This behavior, which is further reflected by the equal values of the scale barrier coefficient α implies that, at long times, the rate of deformation is regulated by the relatively thin surface oxide layer. Further, it is inferred that the zone of internal oxidation, present in the less pure Nickel-201, plays little if any role in determining the deformation behavior under oxidizing conditions.

(3) The steady-state creep rates in helium $\dot{\varepsilon}_S$ are, within experimental error, the same for both grades of nickel at the applied stress levels of both 6.90 and 10.34 MN/m^2.

Although there is a relatively large degree of uncertainty associated with these data, they are interpreted as implying that the steady-state deformation rate is relatively insensitive to solid-solution strengthening.

(4) For both grades of nickel, the steady-state creep rate $\dot{\varepsilon}_S$ after the shorter time of preoxidation (1.44×10^4 sec) is larger than the steady-state creep rate determined from tests in helium; while after the longer time of preoxidation (5.76×10^4 sec), $\dot{\varepsilon}_S$ is much smaller than that determined from tests in helium. The latter effect, which was qualitatively incorporated into the deformation model, is interpreted in terms of the scale layer acting as a barrier to deformation.

The stress-associated rate constant Γ for Nickel-270 at 1000° C may be evaluated from the data of table VIII through the use of equation (17). In this case, average values of $\bar{\beta}^*$ and $\bar{\beta}_0$ may be used in conjunction with the value 10.59 MN/m^2 for σ_g to give $\Gamma = 5.60\times10^{-5}$ m^2/(MN)(sec$^{1/3}$). This value is approximately six times smaller than that determined for Nickel-201, indicating a smaller effect of oxygen-accelerated deformation in Nickel-270.

Parallel to the analysis of the Nickel-201 data, the ratio of the creep rate constants $\beta_{III}/\bar{\beta}_0$ has been determined for Nickel-270 through the use of equation (27). The results of this calculation, shown in figure 24, are based upon average values of the rate constants $\bar{\beta}_0$ and $\bar{\beta}^*$ as well as the value 0.60×10^{-5} second$^{-5/6}$ for the scale barrier coefficient α. The curves shown represent the instantaneous values of the effective Andrade rate constant under oxidizing conditions as a function of the preoxidation time τ relative to the average value of the rate constant as determined from helium atmosphere tests. As the preoxidation time is increased, the rate constant ratios are reduced by factors ranging from 1.5 to 23 with respect to the ratio for the specimen with no preoxidation. Comparison of figure 24 with figure 19 again indicates that the effect of oxygen-accelerated deformation is smaller for Nickel-270 than it is for Nickel-201 and that the enhancement of deformation may be altogether negated at times greater than the order of 10^3 seconds. As in the case of Nickel-201, thicker oxide scale layers on Nickel-270 appear to be better barriers to deformation than do thin layers.

Figure 25, which represents a quantitative check of this latter statement, was constructed on the basis of equation (27), for testing time $t = 0$, by fixing the slope as $-\alpha/\bar{\beta}_0$ and the intercept as $\bar{\beta}^*/\bar{\beta}_0$. The data points shown deviate from the linear graph only inasmuch as individual values of β^* vary from their average. There is, however, a slight negative deviation of the data point representing the specimen preoxidized for 1.44×10^4 seconds. This behavior is in qualitative agreement with that noted for Nickel-201 (see fig. 20). Comparison of these figures also indicates that, while approximately 2×10^3 seconds of preoxidation are required to reduce the value of β_{III} to that of β_0 for Nickel-270, a preoxidation period more than 10 times longer is necessary to similarly reduce the value of β_{III} for Nickel-201. This once again emphasizes the smaller effect of oxygen-accelerated deformation in Nickel-270.

Compilation of Deformation Parameters

The deformation behavior of both grades of nickel tested may be stated in terms of the deformation model and the parameters thereof as determined by experiment and data analyses. Equations (17) and (22) may be combined to give the total creep strain as a function of the testing time

$$\epsilon_T - \delta = \left[\beta_o + \Gamma(\sigma_g - \sigma_a)\right]t^{1/3} - \alpha(\tau + t)^{1/2}t^{1/3} + \dot{\epsilon}_S t \tag{28}$$

wherein the values of β_o, $\dot{\epsilon}_S$, and α are implicitly stress-dependent and the remaining parameters are fixed.

For the purpose of estimating numerical values of $\epsilon_T - \delta$, both the Andrade creep rate constant in helium β_o and the steady-state creep rate constant $\dot{\epsilon}_S$ may be expressed as analytical functions of applied stress using the general form

$$\beta_o = A \exp(B\sigma_a) \tag{29}$$

and

$$\dot{\epsilon}_S = C \exp(D\sigma_a) \tag{30}$$

From the data of table VI, for Nickel-201, the approximate values of the constants in equations (29) and (30) were graphically determined to be: $A = 1.7\times10^{-4}$ second$^{-1/3}$, $B = 0.10$ m^2/MN, $C = 1.7\times10^{-7}$ second^{-1}, and $D = 0.10$ m^2/MN. The scale barrier coefficient α is assumed to be bivalued and equal to 0.60×10^{-5} second$^{-5/6}$ at applied stresses less than σ_g and equal to 0.10×10^{-5} second$^{-5/6}$ at applied stresses greater than σ_g. Thus, for Nickel-201, equation (28) which describes the strain-time behavior becomes

$$\epsilon_T - \delta = \left[1.7\times10^{-4} \exp(0.10\ \sigma_a) + 3.40\times10^{-4}\ (10.59 - \sigma_a)\ \Delta(\mathrm{gas})\right]t^{1/3}$$

$$- \left[0.60 - 0.50\ \Delta(\sigma_a)\right]\times10^{-5}\ \Delta(\mathrm{gas})(\tau + t)^{1/2}\,t^{1/3} + 1.7\times10^{-7}\ t \exp(0.10\ \sigma_a) \tag{31}$$

where the functions $\Delta(\mathrm{gas})$ and $\Delta(\sigma_a)$ are defined as follows:

$$\Delta(\text{gas}) = \begin{cases} 0 \text{ for tests in inert gases} \\ 1 \text{ for tests in oxygen} \end{cases} \tag{32}$$

and

$$\Delta(\sigma_a) = \begin{cases} 0 \text{ for } \sigma_a < \sigma_g \\ 1 \text{ for } \sigma_a > \sigma_g \end{cases} \tag{33}$$

For the case of Nickel-270, the analytical description of the deformation is less certain; however, it may be crudely approximated. From the data of table VIII, the approximate values of the constants given in equations (29) and (30) were graphically determined to be $A = 3\times10^{-4}$ second$^{-1/3}$, $B = 0.10$ m^2/MN, $C = 2\times10^{-7}$ second^{-1}, and $D = 0.10$ m^2/MN. Thus, for Nickel-270, equation (28) which describes the strain-time behavior becomes

$$\epsilon_T - \delta = \left[3\times10^{-4} \exp(0.10\ \sigma_a) + 5.6\times10^{-5}(10.59 - \sigma_a)\ \Delta(\text{gas})\right]t^{1/3}$$
$$-\left[0.60 - 0.50\ \Delta(\sigma_a)\right]\times10^{-5}\ \Delta(\text{gas})(\tau + t)^{1/2}\,t^{1/3} + 2\times10^{-7}t\exp(0.10\ \sigma_a) \tag{34}$$

Metallographic Studies

Structural characterization of materials. - Specimens of both Nickel-201 and Nickel-270 react with oxygen at high temperature to form an external scale of nickel oxide (NiO) which is, in many instances and especially after longer exposure times, composed of two layers (refs. 25, 38, and 39). In addition, oxygen diffuses into the bulk of the metal and there reacts with less-noble impurities to form oxides other than nickel oxide. This latter class of reaction is generally known as internal oxidation (cf. ref. 40).

The major features of the reaction products formed upon oxidation of Nickel-201 are illustrated in the photomicrograph of the cross section shown in figure 26(a). This unstressed specimen which had been exposed to oxygen for 6.51×10^4 seconds at 1000° C exhibited both external and internal oxidation products. The external scale shown is approximately 40 micrometers in thickness and is divided into two layers which are roughly equal in thickness. The outermost scale layer exhibits a definite columnar oxide growth pattern, while the inner layer of oxide shows no well-defined structure at this magnification. Beneath the external scale lies a zone, approximately 80 micrometers in thickness, composed of precipitated oxide particles (internal oxides). No attempt was made to identify these particles chemically; however, they are most probably either manganese oxides or manganese-rich oxides. A similar morphology of internal oxides has previously been noted in oxidized nickel-manganese alloys (ref. 41).

The major features of the structure of oxidized Nickel-270 are illustrated in the photomicrograph of the cross section shown in figure 26(b). This unstressed specimen which has been exposed to oxygen for 6.46×10^4 seconds at 1000° C exhibited both external scale development and a specialized type of subsurface oxidation. The external scale shown is approximately 20 micrometers in thickness and is divided into two layers of unequal thickness. The outermost layer, which accounts for approximately 80 percent of the total scale thickness, exhibits a definite columnar growth pattern, while the grains of the inner oxide layer are more nearly equiaxial.

Subsurface oxidation of Nickel-270, evident in the photomicrograph of figure 26(b), is seen to be associated with the grain boundary network of the nickel matrix. Electron microprobe traces of this material have indicated: (1) that carbon concentrations of 3 atomic percent or more are associated with the unoxidized portions of these boundaries and (2) that the carbon concentration is below detectability limits in both the oxidized portions of the boundaries and the metallic matrix. These observations lead the author to postulate that the carbon is concentrated at the matrix grain boundaries, perhaps during grain growth, and is later oxidized to carbon monoxide gas causing the observed void formation on the grain boundary network. Several of these voids evidently terminate at the surface of the specimen and thereby allow oxygen to be admitted and to oxidize the newly exposed grain surfaces. The depth of such subsurface oxidation is one to two grain diameters or approximately 200 micrometers for the Nickel-270 specimen shown.

Two observations of major importance are emphasized at this time. First, for both Nickel-201 and Nickel-270, approximately 90 percent of the bulk material thickness remains unreacted with oxygen even after the longest times of oxidation. This implies that the prior interpretation of the effect of oxygen upon substrate deformation in terms of perturbations arising from surface reactions alone is probably valid. Second, from inspection of figure 26, it is evident that the less pure Nickel-201 oxidizes to form an external scale at nearly twice the rate k_x of the purer Nickel-270. This implies (1) that the enhancement of deformation by oxidation (as expressed by β_I) should be larger for Nickel-201 than for Nickel-270 as was observed and (2) that, per unit thickness of oxide, the external scale is a stronger barrier to deformation of the purer Nickel-270 than of Nickel-201 (as expressed by the value of α').

Effect of deformation upon specimen structure. - One of the most pronounced effects of high-temperature mechanical deformation upon the structure of test specimens is the production of void space on the grain boundary network of the substrate. This effect is observed both for Nickel-201 and Nickel-270 and is more evident at higher levels of applied stress. Further, the generation of this void space is most pronounced on those portions of the substrate grain boundary network which are oriented nearly normal to the direction of applied stress and associated displacements of the substrate occur parallel to these boundaries. These observations strongly suggest that the high-temperature deformation of nickel occurs, at least in part, by the mechanism of grain boundary shearing. This mode of deformation has been discussed at length elsewhere (refs. 42 to 44).

The photomicrographs of figures 27 and 28 illustrate the effect of deformation upon the structure of Nickel-201 test specimens oxidized at 1000° C as referenced to their companion control specimens. The unstressed control specimen shown in figure 27(a) was exposed to oxygen for 1.98×10^4 seconds and exhibits uniform, planar zones of internal and external oxidation. The companion specimen, similarly exposed but stressed to 6.90 MN/m^2 (shown in fig. 27(b)) also exhibits these planar layers; however, the effect of grain boundary shearing is evident here. It is seen that both the metal and the oxide have experienced a shear displacement in the neighborhood of a grain boundary which is oriented nearly normal to the tensile axis. The continuity of the oxide in the region of this shear implies that the scale is plastic at the test temperature. The void at the end of this boundary furthest from the scale, and in the neighborhood of a three-grain junction, is believed to represent an early stage of void formation by grain boundary shearing.

The specimens of Nickel-201 shown in figure 28 were exposed to oxygen for 1.46×10^4 seconds. It is seen that the degree of void formation in the specimen subjected to an applied load of 13.79 MN/m^2 (fig. 28(b)) is much greater than that observed for the specimen stressed to 6.90 MN/m^2 (fig. 27(b)). Further comparison of these figures reveals (1) that the shear step in the neighborhood of the boundary is larger for the specimen subjected to the larger applied stress and (2) that, in the case of the more highly stressed specimen, oxygen has penetrated the boundary void space in sufficient quantity to allow some internal oxidation of its immediate neighborhood. The structure of the undeformed companion specimen (fig. 28(a)) is quite similar to that of the undeformed specimen illustrated in figure 27(a).

The structures developed in specimens of Nickel-270 exposed to oxygen at 1000° C are qualitatively the same as those exhibited by Nickel-201 with the exception that the zone of internal oxidation is absent and, in its place, there exists the special type of subsurface oxidation noted in the previous section. The photomicrographs of figure 29 show specimens exposed to oxygen for 0.44×10^4 seconds. The unstressed control specimen (fig. 29(a)) shows what appear to be disconnected void and/or oxide sites on the grain boundary network of the metal. The specimen stressed to 10.34 MN/m^2 (fig. 29(b)) exhibits void coalescence and shear displacements which are both probably associated with the grain boundary shearing process.

The results of longer-term oxidation of Nickel-270 are shown in the photomicrographs of figure 30. This specimen pair was exposed to oxygen at 1000° C for 1.08×10^4 seconds. The unstressed control specimen (fig. 30(a)) again exhibits what appear to be disconnected void and/or oxide sites on the grain boundary network of the metal. The specimen stressed to 6.90 MN/m^2 (fig. 30(b)) exhibits some void coalescence and a smaller shear displacement along the boundary than that noted for the specimen tested at 10.34 MN/m^2. As in the case of Nickel-201, the continuity of the scale in the region of the grain boundary shear again implies that the scale is plastic at the test temperature (see fig. 30(b)). An enlarged view of the surface zones of this specimen pair are shown in figure 31. Comparison of these photomicrographs indicates (1) that the metal oxide interface is approximately equally roughened for both the deformed and undeformed specimens, (2) that the dispersed deformation-produced shears which must have passed through the scale of the stressed specimen (fig. 31(b)) apparently did not grossly disrupt the scale continuity, and (3) that the deformed specimen appears to possess a thicker scale than does the undeformed specimen. This final point is the subject of the following section.

Effect of deformation upon oxide scale thickening. - A detailed examination has been made of tested and sectioned specimens of Nickel-270, such as those shown in figure 31, in order to determine the effect of deformation upon the scale thickening process. All specimens were exposed to oxygen at 1000° C in the test chamber used for stress-relaxation tests and all specimens subjected to deformation were nominally stressed to 6.90 MN/m^2.

Several metallographic measurements of the scale formed on both the stressed and the companion control specimens (unstressed) were made. The results of these measurements, presented in table IX, indicate that scale thickening is enhanced by deformation. For those specimens deformed without preoxidation, the total scale thickness x_t is increased by as much as 50 percent and this increase monotonically diminishes as the period of oxidation is increased from 0.72×10^4 to 3.19×10^4 seconds. This behavior indicates that the natural oxide growth process reestablishes itself after the rate of deformation is sufficiently attenuated by the barrier-like properties of the external scale.

Inspection of the thickness determinations for the two component layers which constitute the external scale reveal that the inner scale layer thickness, designated x_2, is at short oxidation times thickened because of deformation. This observation is in qualitative agreement with the concept that the inner scale layer forms as a result of deformation processes acting within the original columnar oxide crystals (see ref. 25). Conversely, it is seen that the outer layer of the external scale, designated x_1, is thickened because of deformation as the time of oxidation under stress is increased. This behavior may be interpreted in terms of a deformation-enhanced transport of material across the interface separating the two scale layers.

For those specimens deformed after the preoxidation treatments, the effect of deformation upon the degree of scale thickening is relatively small and, in fact, the thickness ratios listed for these specimens may differ from unity solely because of statistical variations which arise in their determination. Thus, from all the data of table IX, it is concluded that relatively large rates of substrate deformation, when imposed early in the deformation process, promote a thickening of the external scale. Conversely, relatively small rates of deformation, such as those associated here with preoxidized specimens, do not thicken the scale significantly. It is therefore postulated that the scale thickening which was observed arises as a result of the passage of a large flux of deformation-produced shears through the scale layer.

GENERALIZATION OF RESULTS

The purpose of this section of the report is to qualitatively extend the results of this investigation to areas of consideration for which experimental evidence is lacking. The material which follows is therefore highly speculative in nature and is based mainly on the author's general experience.

It has been shown that, when relatively pure nickel is simultaneously oxidized and deformed at high temperature, the resulting creep deformation may be expressed in terms of certain parameters associated with the formation of an external oxide scale. Conversely, it has been shown, at least in some instances, that the deformation processes associated with the creep of the metal-scale composite affect the growth of surface oxide layers. It is therefore concluded that, for testing regimes similar to that under consideration, the oxidation and deformation processes are truly coupled in that an alteration of one aspect alters the other. Further, it is postulated that these coupled processes are general in nature and may be applied, with change of degree, both to other types of materials and to other types of deformation environments.

As expressed by the equations of the deformation model, there are two major parameters of the scale which influence the composite scale-substrate deformation: (1) the barrier coefficient α which contains both the unit strength of the barrier α' and the rate of barrier formation k_x and (2) the natural grain boundary pressure of the growing oxide σ_g. The surface barrier concept has been shown by others to be applicable over wide ranges of material types (refs. 1 to 13) and the growth pressurization of oxide scales has been suggested as a general phenomenon (refs. 25 and 45); thus, the creep deformation of many oxidizing metallic substrates should, in principle, be expressible in terms of equations (24) and (25) of the proposed model.

The ability of scales on metals and alloys other than nickel to act as effective deformation barriers is difficult to predict and some general considerations are in order. Most oxides are less ductile than nickel oxide under conditions of creep and, although they may act as deformation barriers with a larger unit strength α', this same lack of ductility makes these scales more liable to mechanically induced faults with an associated total local loss of barrier property. Further, the rate of barrier formation k_x for these scales is quite possibly more sensitive to imposed deformation than was the nickel oxide of this investigation and, in fact, variations in the type of scaling rate law may well be expected. If either of these cases prevail, then one must recast the deformation equations to contain an explicit functional dependence of k_x upon, for example, the total strain rate $\dot{\epsilon}_T$ and must, therefore, deal with a set of transcendental deformation equations. Unfortunately, almost no information is presently available concerning this type of functional relation between the deformation and the scaling rate of metals or alloys.

If it is assumed that the proposed deformation model is generally applicable, the creep of oxidizing substrates will also depend strongly upon the relative value of the difference between the oxide grain boundary pressure σ_g and the magnitude of the applied creep stress σ_a. The value of σ_g, in turn, is believed to depend upon the oxide grain size in that, qualitatively, smaller grain sizes should produce larger values of grain boundary pressure. Materials of engineering importance for high-temperature application in many cases exhibit external scales of chromia or alumina which are composed of oxide grains very much smaller in dimension than those of nickel oxide. The values of σ_g for these scales are postulated to be commensurately larger than that of nickel oxide and, in fact, are possibly so large that in most instances σ_g exceeds σ_a. Thus, it is proposed that many high-temperature engineering materials are presently being used in environments in which oxidation at least initially accelerates deformation. A case in point which tends to substantiate this argument is presented in a recently reported study of the oxidation of the cobalt-base superalloy L-605 (ref. 46). In this instance, the growth pressure developed in chromia scales was cited as the cause for the mechanical disruption of the relatively strong alloy substrate.

As the complexity of the environment is increased, the projection of possible material response to service loads becomes commensurately more difficult. Thus, as one progresses through the gamut of high-temperature testing from creep (constant load) to tensile loading (monotonically increasing load) to fatigue (alternating load) and, finally, to applications such as turbine engine tests (complex load-temperature histories), it is apparent that the parameters associated with scale formation must be known as functions of more and more variables in order that a closed-form solution of the deformation behavior, analogous to that of equation (24), be obtained. The author hopes that the ideas contained in this report may serve as the kernel for the solution of such more complex interaction problems.

CONCLUSION

It is concluded that the high-temperature oxidation and deformation processes in nickel are truly coupled. It is probable that this concept of coupled processes can usefully be extended to other metals and alloys.

SUMMARY OF RESULTS

An investigation was conducted in order to determine the effect of oxide scale formation on the deformation behavior of unalloyed nickel at high temperature. Two grades of material, Nickel-201 and Nickel-270, were tested by constant load and stress-relaxation techniques at 1000° C in both inert gases and oxygen. Applied stress levels ranging from 6.90 to 13.79 MN/m^2 were imposed for total test times of up to 6.5×10^4 seconds. The following results were obtained:

1. A model was derived describing the high-temperature deformation of unalloyed nickel in terms of parameters associated with the surface oxidation product. The qualities of the surface scale which affect deformation were found to be its natural growth stress (grain boundary pressure) and its barrier-like properties.

2. A graphical technique was devised, based on pairs of conjugate curves, with which experimental deformation data were interpreted in terms of the equations of the model. By such analyses, deformation parameters were evaluated to give a closed-form solution for the strain (and strain rate) of nickel as a function of gaseous environment, applied stress, preoxidation time, and time of deformation.

3. Observed discontinuities in the deformation of nickel, associated with initial oxygen reaction at the specimen surface, were attributed to the grain boundary pressure of the surface oxide. It was shown that the transient deformation of nickel is initially enhanced by a surface oxide layer so long as the applied stress is less than the grain boundary pressure of nickel oxide and that the transient deformation of nickel is retarded by a surface oxide layer so long as the applied stress is greater than the grain boundary pressure of nickel oxide.

4. By use of an iterative graphical method based upon the deformation model, the value of the grain boundary pressure for nickel oxide was found to be 10.59 MN/m^2 at 1000° C. This value agrees well with that determined previously by a totally different technique and the scheme of determination used herein appears to be applicable for other metal-metal oxide systems.

5. The transient deformation of nickel is, at long oxidation times, retarded by the presence of a surface oxide layer and the total deformation of nickel is grossly reduced by long-term preoxidation treatments. Similarly, both the transient and steady-state deformation rates tend toward zero as the time of preoxidation is extended. These long-term effects are here associated with the barrier-like qualities of the scale.

6. The thickness of the scale layer developed on Nickel-270 is enhanced by substrate deformation imposed early in the oxidation process, but is relatively unaffected by

deformation after long-term oxidation. Thus, a change in the mode of scale growth is to be associated with relatively high rates of substrate deformation.

Lewis Research Center,
National Aeronautics and Space Administration,
Cleveland, Ohio, February 18, 1969,
129-03-07-01-22.

REFERENCES

1. Pickus, M. R.; and Parker, E. R.: Creep as a Surface Dependent Phenomenon. Symposium on Corrosion of Materials at Elevated Temperatures. Spec. Tech. Publ. No. 108, ASTM, 1950, pp. 26-33.
2. Sinnott, M. J.: The Influences of Surfaces on the Properties of Materials. Properties of Crystalline Solids. Spec. Tech. Publ. No. 283, ASTM, 1960, pp. 28-39.
3. Kramer, Irvin R.; and Demer, Louis J.: Effects of Environment on Mechanical Properties of Metals. Progress in Materials Science. Vol. 9, no. 3. Pergamon Press, 1961.
4. Roscoe, R.: The Plastic Deformation of Cadmium Single-Crystals. Phil. Mag., Ser. 7, vol. 21, Feb. 1936, suppl., pp. 399-406.
5. Andrade, E. N. daC.; and Randall, R. F. Y.: Surface Effects with Single Crystal Wires of Cadmium. Nature, vol. 162, Dec. 4, 1948, pp. 890-891.
6. Andrade, E. N. daC.; and Randall, R. F. Y.: The Rehbinder Effect. Nature, vol. 164, Dec. 31, 1949, p. 1127.
7. Harper, S.; and Cottrell, A. H.: Surface Effects and the Plasticity of Zinc Crystals. Proc. Phys. Soc., vol. 63B, pt. 5, May 1950, pp. 331-338.
8. Menter, J. W.; and Hall, E. O.: Surface Effects on the Creep of Cadmium Single Crystals. Nature, vol. 165, Apr. 15, 1950, pp. 611-612.
9. Barrett, Charles S.: An Abnormal After-Effect in Metals. Acta Met., vol. 1, no. 1, Jan. 1953, pp. 2-7.
10. Phillips, D. J.; and Thompson, N.: Surface Effects in Creep of Cadmium Crystals. Proc. Phys. Soc., vol. 63B, pt. 11, Nov. 1950, pp. 839-847.
11. Head, A. K.: The Interaction of Dislocations and Boundaries. Phil. Mag., vol. 44, no. 348, Jan. 1953, pp. 92-94.

12. Sweetland, E. D.; and Parker, E. R.: Effect of Surface Condition on Creep of Some Commercial Metals. J. Appl. Mech., vol. 20, no. 1, Mar. 1953, pp. 30-32.

13. Head, A. K.: The Interaction of Dislocations with Boundaries and Surface Films. Austral. J. Phys., vol. 13, no. 2a, July 1960, pp. 278-283.

14. Thielemann, R. H.; and Parker, E. R.: Fracture of Steels at Elevated Temperatures after Prolonged Loading. Trans. AIME, vol. 135, 1939, pp. 559-582.

15. Shepard, O. C.; and Schalliol, W.: The Effect of Environment on the Stress-Rupture Properties of Metals at Elevated Temperatures. Symposium on Corrosion of Materials at Elevated Temperatures. Spec. Tech. Publ. No. 108, ASTM, 1950, pp. 34-38.

16. Shahinian, Paul: Effect of Environment on Creep-Rupture Properties of Some Commercial Alloys. Trans. ASM, vol. 49, 1957, pp. 862-882.

17. Shahinian, Paul; and Achter, M. R.: Temperature and Stress Dependence of the Atmosphere Effect on a Nickel-Chromium Alloy. Trans. ASM, vol. 51, 1959, pp. 244-255.

18. Widmer, Robert; and Grant, Nicholas J.: The Role of Atmosphere in the Creep-Rupture Behavior of 80 Ni-20 Cr Alloys. J. Basic Eng., vol. 82, no. 4, Dec. 1960, pp. 882-886.

19. Danek, G. J., Jr.; Smith, H. H.; and Achter, M. R.: High-Temperature Fatigue and Bending Strain Measurements in Controlled Atmospheres. Proc. ASTM, vol. 61, 1961, pp. 775-788.

20. Shaninian, P.; and Achter, M. R.: A Comparison of the Creep-Rupture Properties of Nickel in Air and Vacuum. Rep. 5036, Naval Research Lab., Oct. 18, 1957.

21. Shahinian, P.; and Achter, M. R.: Creep-Rupture of Nickel of Two Purities in Controlled Environments. Rep. 5880, Naval Research Lab., Jan. 22, 1963.

22. Phalnikar, C. A.; and Baldwin, W. M., Jr.: The Scaling of Zirconium in Air. Proc. ASTM, vol. 51, 1951, pp. 1038-1060.

23. Jaenicke, Walther; and Leistikow, Siegfried: Mechanical Stresses in the Formation of Oxide Layers. I. Oxidation of Copper. Z. Physik. Chem., N. F., vol. 15, 1958, pp. 175-195.

24. Pawel, R. E.; Cathcart, J. V.; and Campbell, J. J.: Stress Generation in Tantalum During Oxidation. J. Electrochem. Soc., vol. 110, no. 6, June 1963, pp. 551-557.

25. Wolf, James S.: An Investigation of the Effect of Specimen Geometry on the Oxidation of Nickel at Elevated Temperatures. Ph. D. Thesis, Univ. Florida, 1965.

26. Becker, G. F.; and Day, A. L.: The Linear Force of Growing Crystals. Proc. Wash. Acad. Sci., vol. 7, 1905, pp. 283-288.

27. Wright, F. E.; and Hostetter, J. C.: The Thermodynamic Reversibility of the Equilibrium Relations Between a Strained Solid and its Liquid. J. Wash. Acad. Sci., vol. 7, July 19, 1917, pp. 405-417.

28. Taber, S.: Pressure Phenomena Accompanying the Growth of Crystals. Proc. Nat. Acad. Sci., vol. 3, 1917, pp. 297-302.

29. Correns, Carl W.: Growth and Dissolution of Crystals Under Linear Pressure. Disc. Faraday Soc., no. 5, 1949, pp. 267-271.

30. Tylecote, R. F.: Factors Influencing the Adherence of Oxides on Metals. J. Iron and Steel Inst., vol. 196, pt. 2, Oct. 1960, pp. 135-141.

31. Wagner, Carl; and Grünewald, Karl: Theory of the Tarnishing Process. III. Z. Physik. Chem., vol. 40B, 1938, pp. 455-475.

32. Moore, Walter J.; and Lee, James K.: Kinetics of the Formation of Oxide Films on Nickel Foil. Trans. Faraday Soc., vol. 48, 1952, pp. 916-920.

33. Gulbransen, Earl A.: Classical Theory of Diffusion and the Oxidation of Metals. Ann. N. Y. Acad. Sci., vol. 58, 1954, pp. 830-842.

34. Lombard, C. A.: The Kinetics of Oxidation of High Purity Nickel. AFML TR-65-53, Air Force Systems Command, May 1965. (Available from DDC as AD-467108.)

35. Andrade, E. N. daC.: On the Viscous Flow in Metals and Allied Phenomena. Proc. Roy. Soc., ser. A, vol. 84, June 9, 1910, pp. 1-12.

36. Andrade, E. N. daC.: The Flow in Metals Under Large Constant Stresses. Proc. Roy Soc., ser. A, vol. 90, July 1, 1914, pp. 329-342.

37. Cottrell, A. H.; and Aytekin, V.: Andrade's Creep Law and the Flow of Zinc Crystals. Nature, vol. 160, Sept. 6, 1947, pp. 328-329.

38. Vasyutinskiy, B. M.; and Kartmazov, G. N.: Mechanism of Nickel Oxidation. Phys. Met. Metallog., vol. 15, no. 1, 1963, pp. 120-122.

39. Seybolt, A. U.: Oxidation of Metals. Adv. Phys., vol. 12, no. 45, 1963, pp. 1-43.

40. Darken, L. S.: Diffusion in Metal Accompanied by Phase Change. Trans. AIME, vol. 150, 1942, pp. 157-171.

41. Wolf, James S.; Weeton, John W.; and Freche, John C.: Observations of Internal Oxidation in Six Nickel-Base Alloy Systems. NASA TN D-2813, 1965.

42. McLean, Donald: Grain Boundaries in Metals. Clarendon Press, Oxford, 1957, pp. 256-295.

43. Cottrell, A. H.: Intercrystalline Creep Fractures. Iron Steel Inst. Spec. Rept. no. 70, 1961, pp. 1-18.

44. Stevens, R. N.: Grain-Boundary Sliding in Metals. J. Inst. Metals Bull. Met. Rev., vol. 94, no. 10, 1966, pp. 129-142.

45. Tylecote, R. F.: Internal Stresses in Oxide Films During Growth. Colloq. Intern. Centre. Nat. Rech. Sci. (Paris), no. 122, 1965, pp. 241-247.

46. Wolf, James S.; and Sandrock, Gary D.: Some Observations Concerning the Oxidation of the Cobalt-Base Superalloy L-605 (HS-25). NASA TN D-4715, 1968.

TABLE I. - NOMINAL COMPOSITIONS OF NICKEL-201 AND NICKEL-270[a]

Element	Weight percentage
Nickel-201	
Nickel (+ cobalt)	99.40
Manganese	.25
Iron	.15
Carbon	.06
Silicon, copper	.05 each
Sulfur	.005
Nickel-270	
Nickel	99.98
Carbon	.005
Iron	<.005
Others	<.003 each including cobalt

[a] Compositions reported by supplier.

TABLE II. - ELECTROPOLISHING CONDITIONS USED IN SPECIMEN PREPARATION (REF. 25)

Polishing solution	817 cc H_3PO_4 134 cc H_2SO_4 40 cc H_2O - distilled 156 g CrO_3 - taken into solution
Cathode	Nickel-201 cylinder
Bath temperature, °C	35 to 45
Current density, A/cm^2	0.2 to 0.4
Polishing time, sec	500 to 1000

TABLE III. - METHOD OF DATA ANALYSIS FOR CONSTANT LOAD CREEP TESTS

Time, sec	Time interval, sec	Average time, sec	Total strain	Strain increment	Strain rate, sec^{-1}
t_i	-------	----------	$(\epsilon_T)_i$	-------------	-------------
----	$t_{i+1} - t_i$	$t_i + \frac{t_{i+1} - t_i}{2}$	------	$(\epsilon_T)_{i+1} - (\epsilon_T)_i$	$\frac{(\epsilon_T)_{i+1} - (\epsilon_T)_i}{t_{i+1} - t_i}$
t_{i+1}	-------	----------	$(\epsilon_T)_{i+1}$	-------------	-------------

TABLE IV. - METHOD OF DATA ANALYSIS FOR STRESS-RELAXATION CREEP TESTS

Number of relaxation cycles	Nominal strain increment	Total strain	Time interval, sec	Total elapsed time, sec	Average time of measurement, sec	Strain rate, sec^{-1}
j(N)	ϵ_N	$(j)(\epsilon_N)$	t_j	$\sum_1^j t_j$	------------	---
--------	---	---------	---	----	$\sum_1^i t_j + \frac{t_{j+1}}{2}$	$\frac{\epsilon_N}{t_{j+1}}$
(j + 1)(N)	ϵ_N	$(j + 1)(\epsilon_N)$	t_{j+1}	$\sum_1^{j+1} t_j$	------------	---

TABLE V. - CHEMICAL AND ELECTROLYTIC ETCHING PROCESSES USED IN THE METALLOGRAPHIC PREPARATION OF SECTIONED SPECIMENS

Etching solution	Remarks
Chemical etching process for Nickel-201	
12 cc HNO_3 36 cc HCl 32 cc of aqueous solution saturated with $CuCl_2$ 16 cc CH_3CH_2OCOOH	Age approximately 10^4 seconds at room temperature. Swab etch at room temperature.
Chemical etching process for Nickel-270 (ref. 25)	
25 cc HNO_3 25 cc CH_3COOH - glacial 50 cc H_2O - distilled	Immersion etch at room temperature for 30 to 120 seconds.
Electrolytic etching process for nickel oxide (ref. 25)	
10 cc CH_3COOH - glacial 10 cc HF 40 cc H_2O - distilled	Stainless-steel cathode. 5 volts (open circuit) at room temperature for 10 to 120 seconds. This process follows chemical etch for Nickel-201 or Nickel-270.

TABLE VI. - SUMMARY OF CONSTANT LOAD CREEP TEST PARAMETERS FOR NICKEL-201

AS DETERMINED BY CONJUGATE CURVE ANALYSIS

Applied stress, σ_a, MN/m^2	Nominal specimen thickness, mm	Andrade creep rate constant in helium, β_o, sec$^{-1/3}$		Average Andrade creep rate constant in helium, $\overline{\beta}_o$, sec$^{-1/3}$	Andrade creep rate constant in oxygen, β^*, sec$^{-1/3}$		Average Andrade creep rate constant in oxygen, $\overline{\beta}^*$, sec$^{-1/3}$	Steady-state creep rate in helium, $\dot{\varepsilon}_S$, sec^{-1}	Scale barrier coefficient in oxygen, α, sec$^{-5/6}$
		Strain rate data	Strain data		Strain rate data	Strain data			
6.90	3.2	8.01×10^4	8.09×10^4	8.05×10^4	20.9×10^4	20.7×10^4	20.8×10^4	1.00×10^6	0.48×10^5
6.90	1.6	8.91	8.85	8.88	20.7	21.2	21.0	.20	.60
10.34	3.2	21.5	21.9	21.7	22.7	22.8	22.8	2.25	.60
13.79	3.2	42.7	42.0	42.4	33.6	31.8	32.7	3.75	.10

TABLE VII. - SUMMARY OF STRESS-RELAXATION CREEP TEST PARAMETERS FOR NICKEL-201 STRESSED TO 6.90 MN/m^2 AT 1000° C

Test atmosphere	Pre-oxidation time, τ, sec	Andrade creep rate constant, β_o or β^*, sec$^{-1/3}$		Average Andrade creep rate constant, $\bar{\beta}_o$ or $\bar{\beta}^*$, sec$^{-1/3}$	Steady-state creep rate by conjugate curve analysis, $(\mathring{\epsilon}_S)_{cc}$, sec^{-1}	Steady-state creep rate by curve tangent analysis, $(\mathring{\epsilon}_S)_{tan}$, sec^{-1}	Steady-state creep rate ratio, $\frac{(\mathring{\epsilon}_S)_{cc}}{(\mathring{\epsilon}_S)_{tan}}$	Scale barrier coefficient (assumed value) α, sec$^{-5/6}$
		Strain rate data	Strain data					
Helium	---------	5.19×10^4	5.13×10^4	5.16×10^4	0.1×10^6	1.6×10^6	0.06	--------
Oxygen	1.44×10^{-4}	9.45	9.40	9.43	1.4	2.0	.70	0.60×10^5
Oxygen	5.76	15.5	15.4	15.5	.4	.41	.98	.60

TABLE VIII. - SUMMARY OF STRESS-RELAXATION CREEP PARAMETERS FOR NICKEL-270 TESTED AT 1000° C

Test atmosphere	Pre-oxidation time, τ, sec	Applied stress, σ_a, MN/m^2	Andrade creep rate constant, β_o or β^*, sec$^{-1/3}$		Average Andrade creep rate constant, $\bar{\beta}_o$ or $\bar{\beta}^*$, sec$^{-1/3}$	Steady-state creep rate by conjugate curve analysis, $\mathring{\epsilon}_S$, sec^{-1}	Scale barrier coefficient (assumed value), α, sec$^{-5/6}$
			Strain rate data	Strain data			
Helium	0×10^{-4}	6.90	14.2×10^4	14.1×10^4	14.2×10^4	0.2×10^6	--------
Argon	0	6.90	12.4	12.7	12.6	1.0	--------
Argon	0	6.90	12.7	13.0	12.9	1.0	--------
Helium	0	[a]6.90	10.0	10.2	10.1	0	--------
Oxygen	1.44	6.90	14.8	14.7	14.8	3.0	0.60×10^5
Oxygen	5.76	6.90	15.7	15.8	15.8	0	.60
Helium	0	10.34	23.8	23.6	23.7	2.0	--------

[a] Instantaneously prestressed to 7.75 MN/m^2 at 1000° C just prior to testing at 6.90 MN/m^2.

TABLE IX. - SUMMARY OF SCALE THICKNESS DETERMINATIONS FOR STRESSED AND UNSTRESSED SPECIMENS OF NICKEL-270 OXIDIZED AT 1000° C

Applied stress, σ_a, MN/m^2	Total time in oxygen, sec	Pre-oxidation time, τ, sec	Total scale thickness, x_t, μm	Ratio of total scale thicknesses (stressed/ unstressed)	Thickness of outer scale layer, x_1, μm	Ratio of outer scale layer thicknesses (stressed/ unstressed)	Thickness of inner scale layer, x_2, μm	Ratio of inner scale layer thicknesses (stressed/ unstressed)
6.90	0.72×10^{-4}	0×10^{-4}	5.86	1.48	2.96	1.28	2.91	1.76
0	.72	0	3.97		2.32		1.65	
6.90	1.08	0	8.15	1.27	4.71	1.42	3.45	1.12
0	1.08	0	6.42		3.33		3.09	
6.90	3.19	0	13.90	1.14	9.97	1.54	3.99	.84
0	3.19	0	11.22		6.49		4.74	
6.90	3.25	1.44	11.10	.85	6.00	.91	5.11	.79
0	3.25	1.44	13.04		6.58		6.46	
6.90	6.46	5.76	21.41	1.02	17.35	.99	4.07	1.14
0	6.46	5.76	21.00		17.44		3.56	

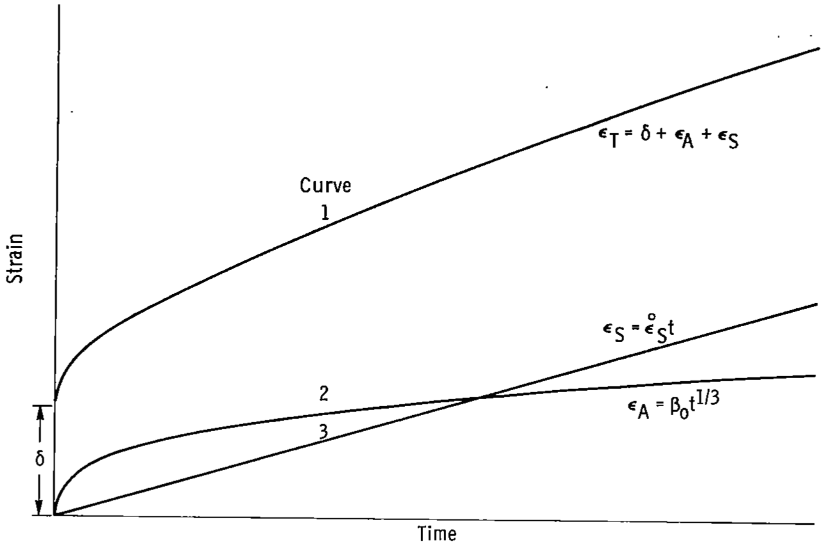

Figure 1. - Typical strain-time diagram showing total strain ϵ_T as sum of time-independent strain δ, steady-state creep strain ϵ_S, and Andrade (transient) creep strain ϵ_A.

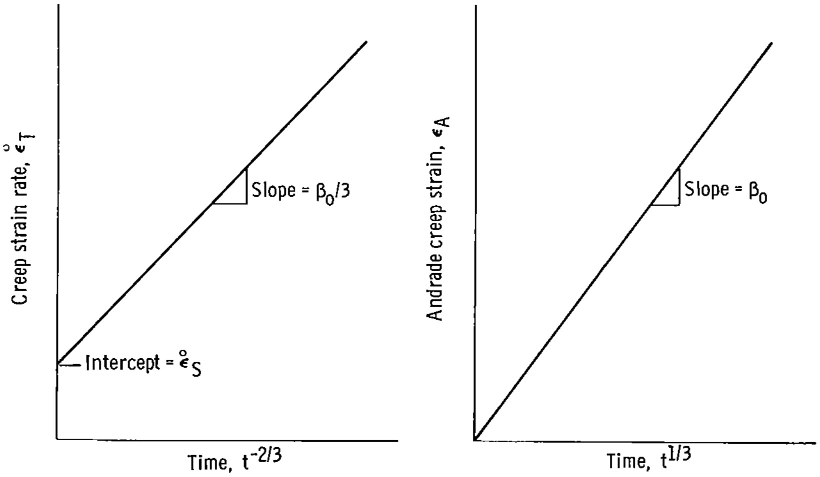

(a) Strain rate-time relation.

(b) Strain-time relation.

Figure 2. - Conjugate strain rate-time and strain-time diagrams from which Andrade creep rate constant β_0 and steady-state creep rate $\overset{\circ}{\epsilon}_S$ may be determined for unoxidized metal specimen.

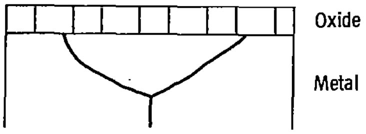

(a) Unstressed initial scale layer.

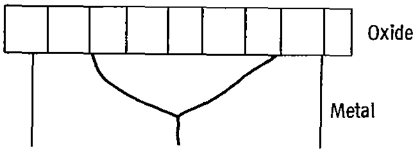

(b) Hypothetical scale growth without constraint of metal-oxide interface.

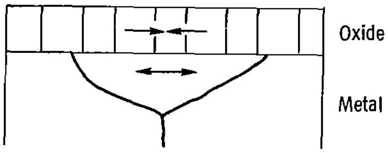

(c) Hypothetical scale growth with constraint of metal-oxide reapplied.

Figure 3. - Illustration of development of lateral compressive stress in scale layer leading to extension of metallic substrate.

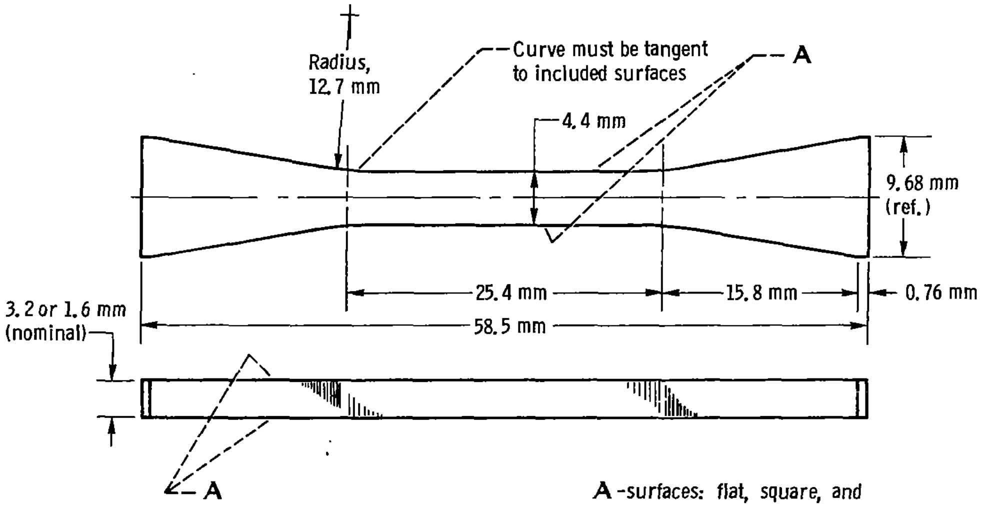

A -surfaces: flat, square, and parallel to within 0.05 mm

CD-10331-17

Figure 4. - Tensile creep specimen used in this investigation.

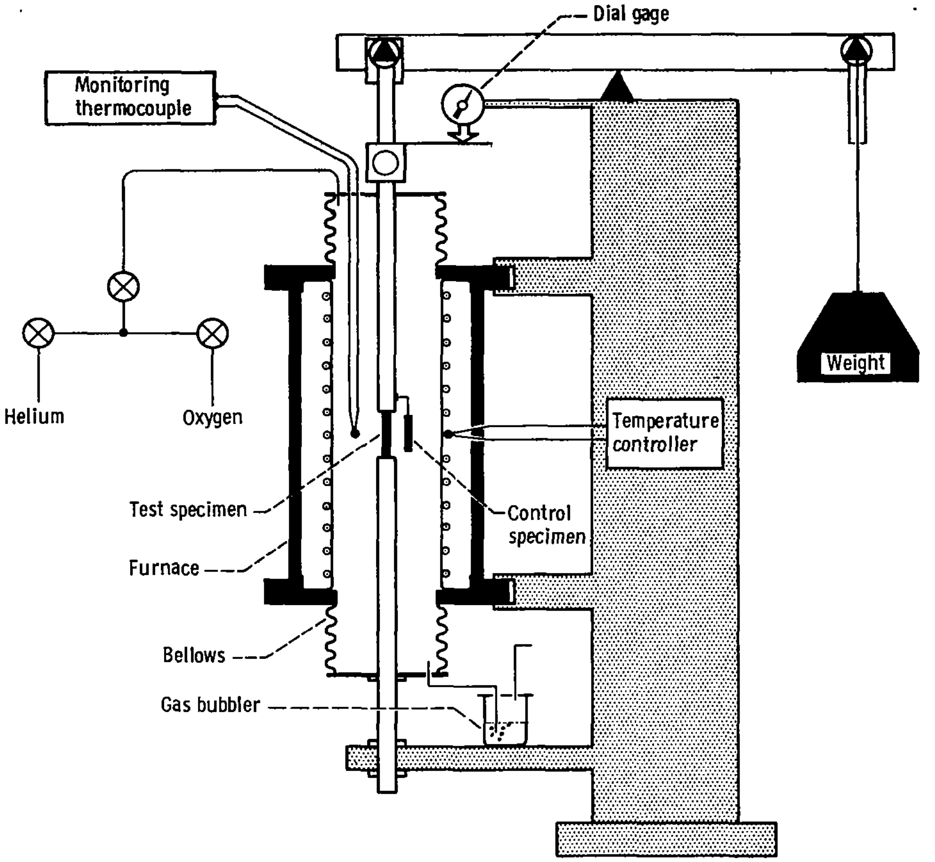

CD-10332-17

Figure 5. - Constant load creep apparatus.

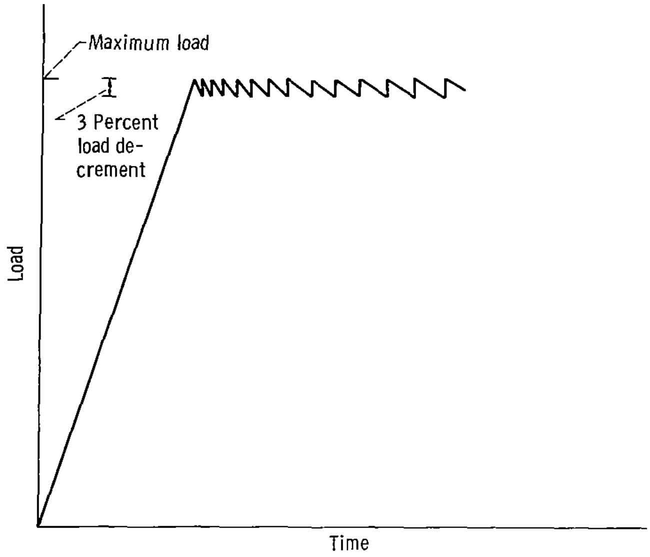

Figure 6. - Stress-relaxation curve showing relation of timing intervals and relaxation cycles.

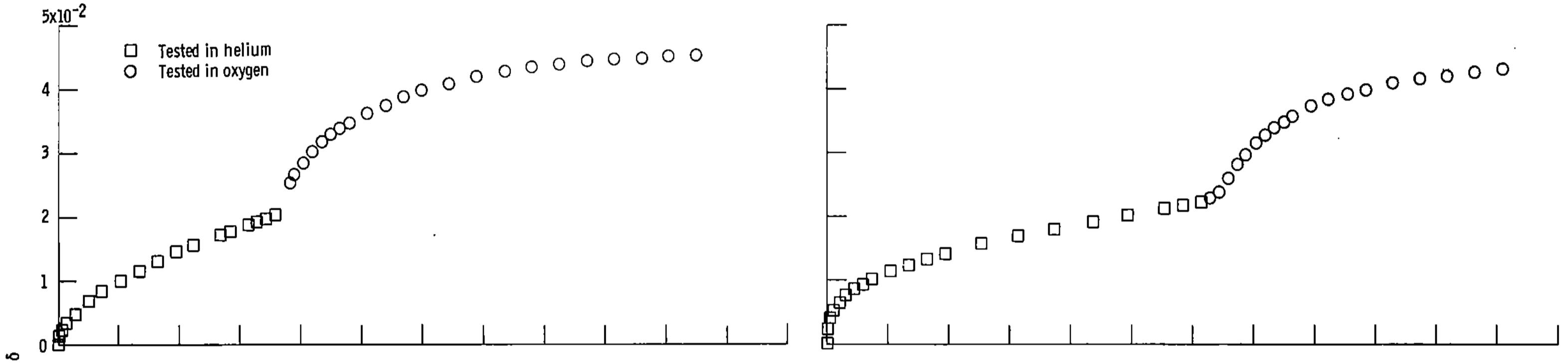

(a) Stressed at 6.90 MN/m^2; nominal thickness, 3.2 millimeters.

(b) Stressed at 6.90 MN/m^2; nominal thickness, 1.6 millimeters.

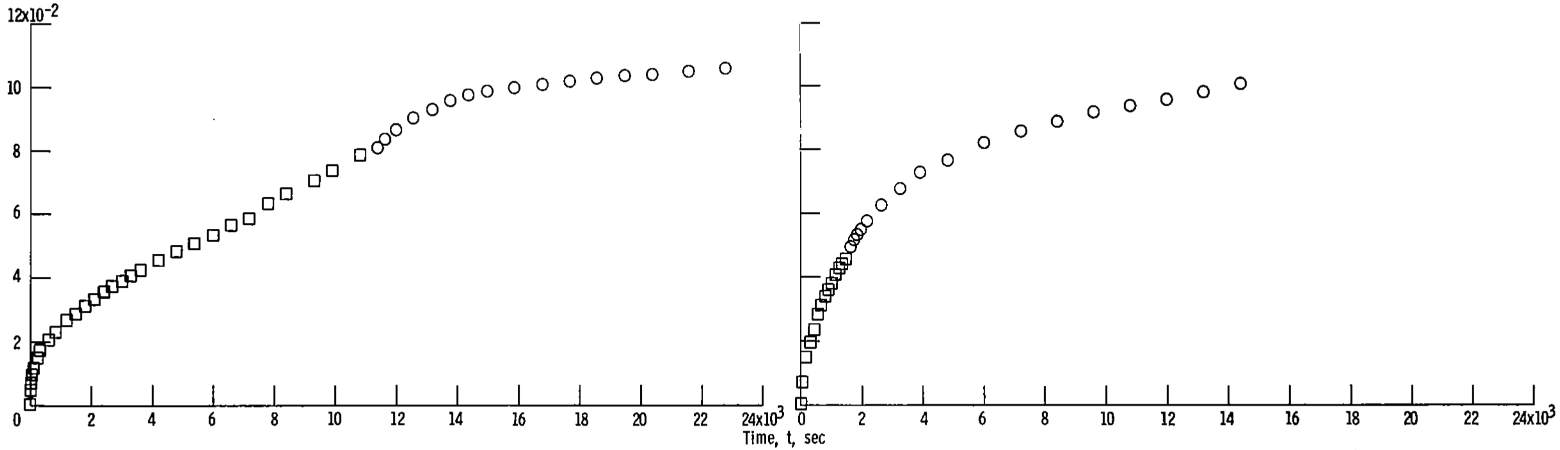

(c) Stressed at 10.34 MN/m^2; nominal thickness, 3.2 millimeters.

(d) Stressed at 13.79 MN/m^2; nominal thickness, 3.2 millimeters.

Figure 7. - Deformation behavior of Nickel-201 at 1000° C initially in helium and, subsequently, after admission of oxygen to test chamber. (Note deformation increments associated with oxygen admission.)

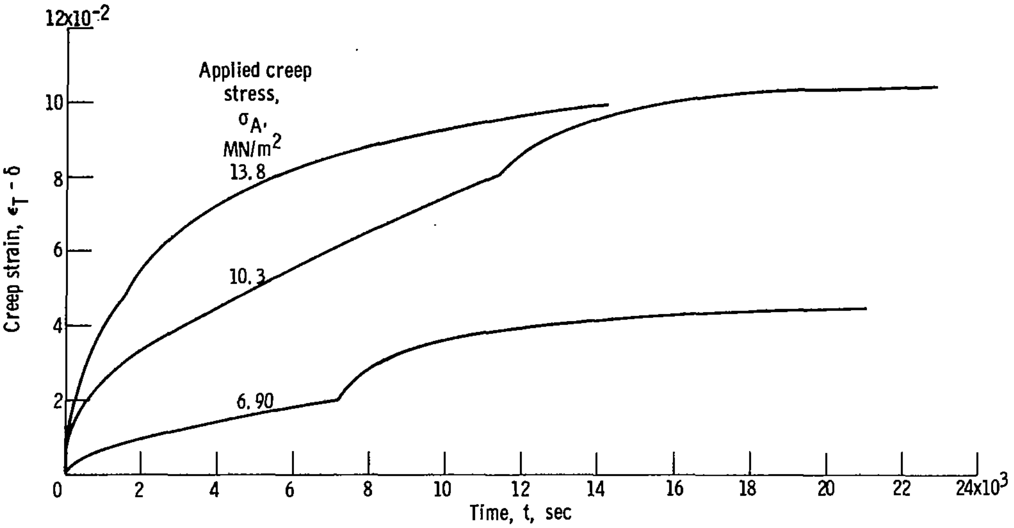

Figure 8. - Curves representing data of figures 7(a), (c), and (d) which illustrate that relative magnitude of deformation increment due to presence of oxygen diminishes with increasing applied stress for 3.2-millimeter-thick specimens of Nickel-201 tested at 1000° C.

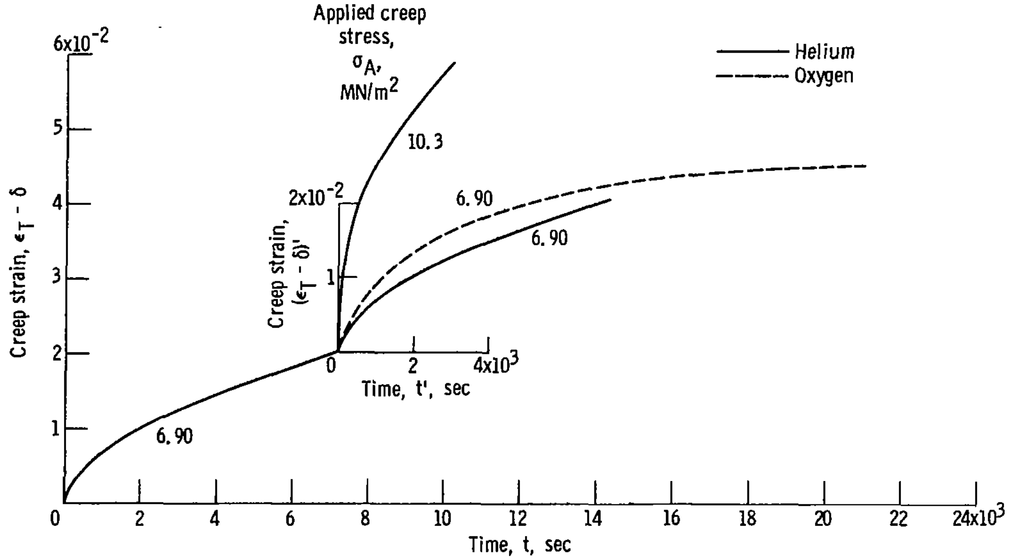

Figure 9. - Comparison of strain increment developed by oxygen in Nickel-201 at 1000° C with deformation curves for virgin material in helium. (Primed coordinate system shown here is employed in analysis of deformation behavior under oxidizing conditions.)

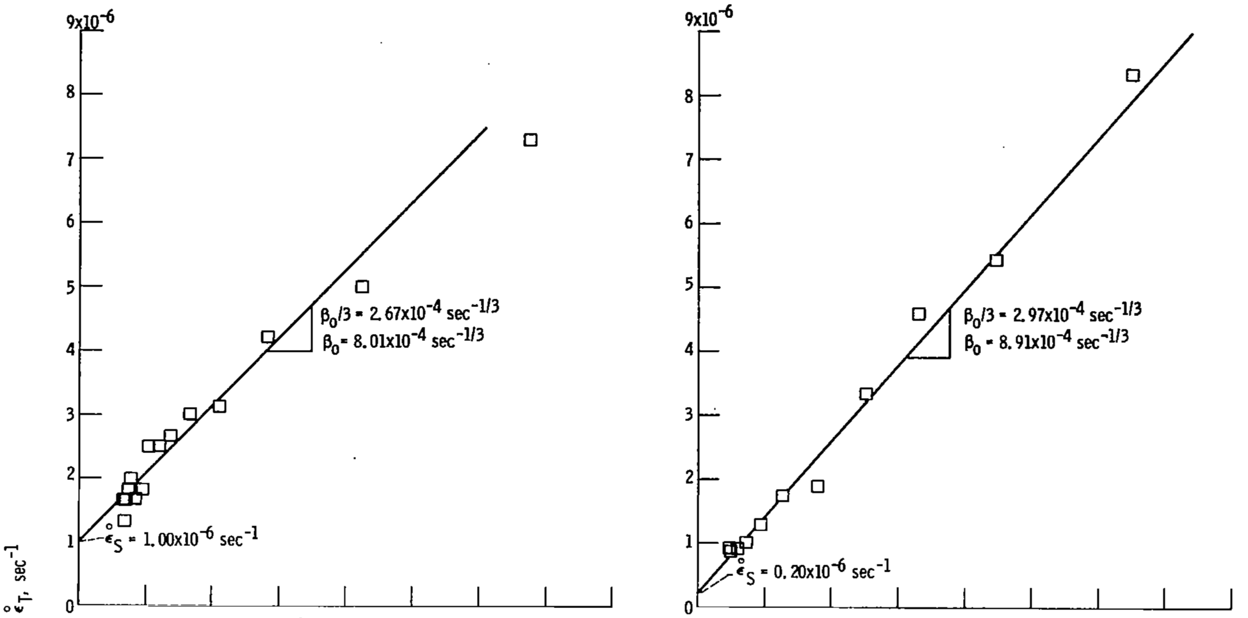

(a) Stressed at 6.90 MN/m^2; nominal thickness, 3.2 millimeters.

(b) Stressed at 6.90 MN/m^2; nominal thickness, 1.6 millimeters.

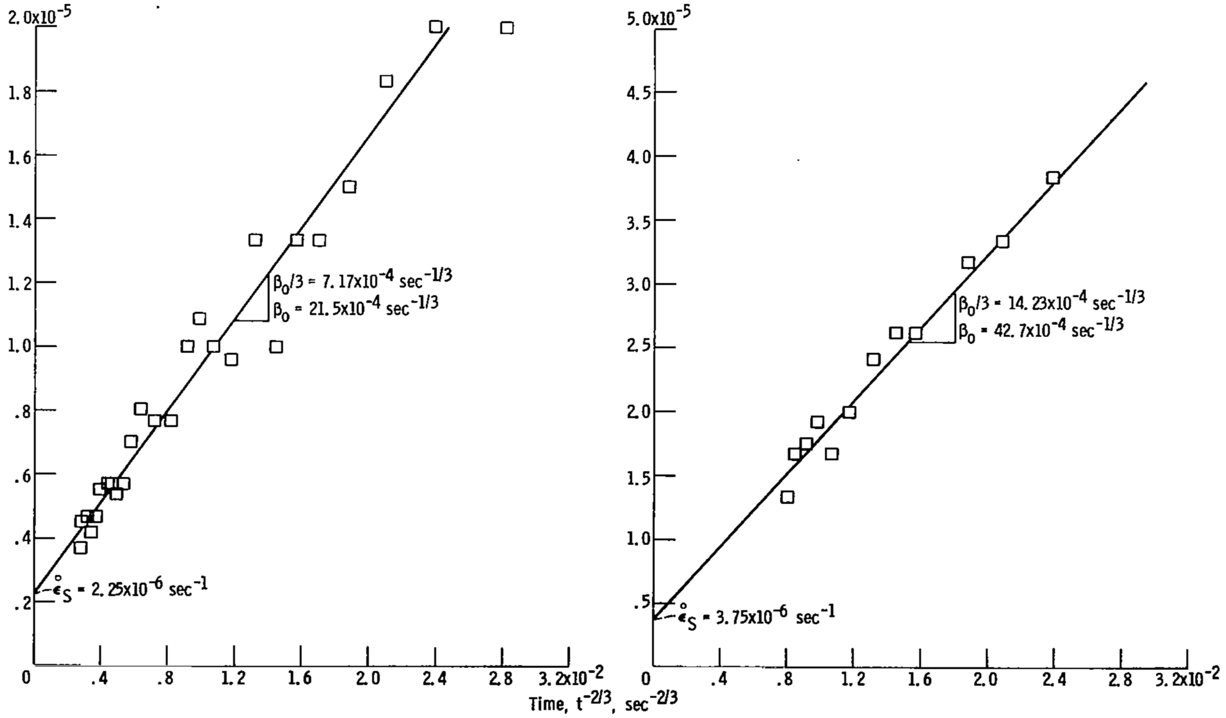

(c) Stressed at 10.34 MN/m^2; nominal thickness, 3.2 millimeters.

(d) Stressed at 13.79 MN/m^2; nominal thickness, 3.2 millimeters.

Figure 10. - Strain rate-time relations for deformation behavior of Nickel-201 in helium at 1000° C.

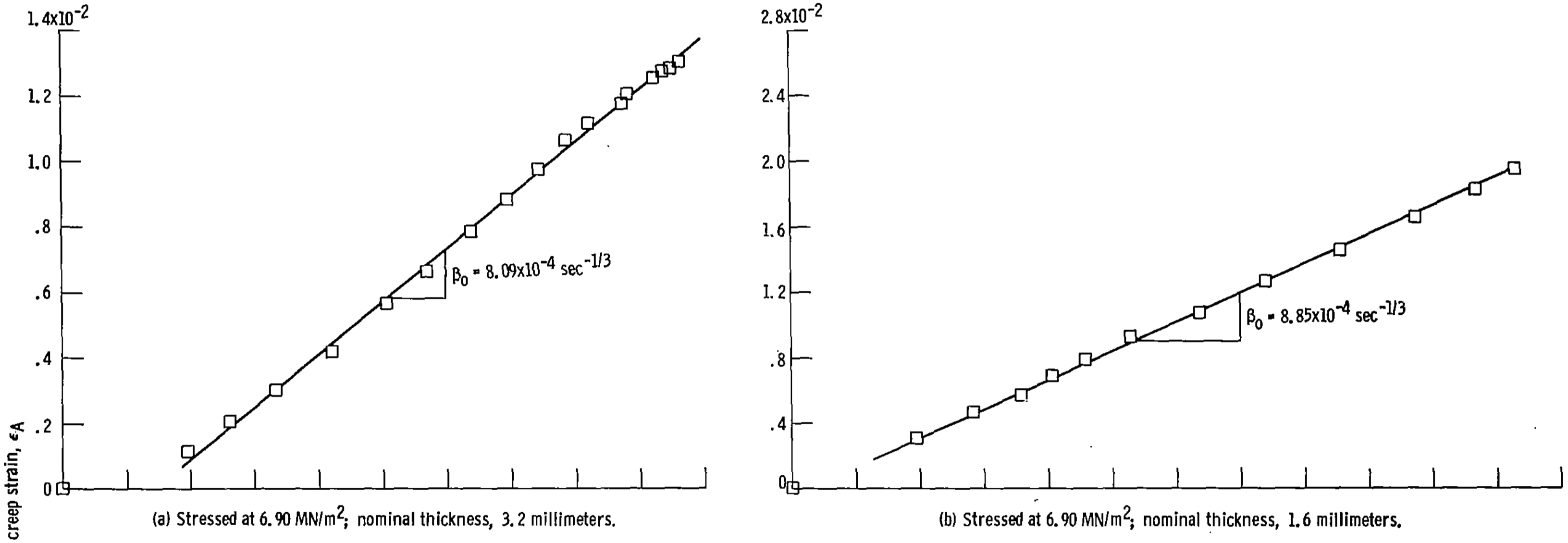

(a) Stressed at 6.90 MN/m^2; nominal thickness, 3.2 millimeters.

(b) Stressed at 6.90 MN/m^2; nominal thickness, 1.6 millimeters.

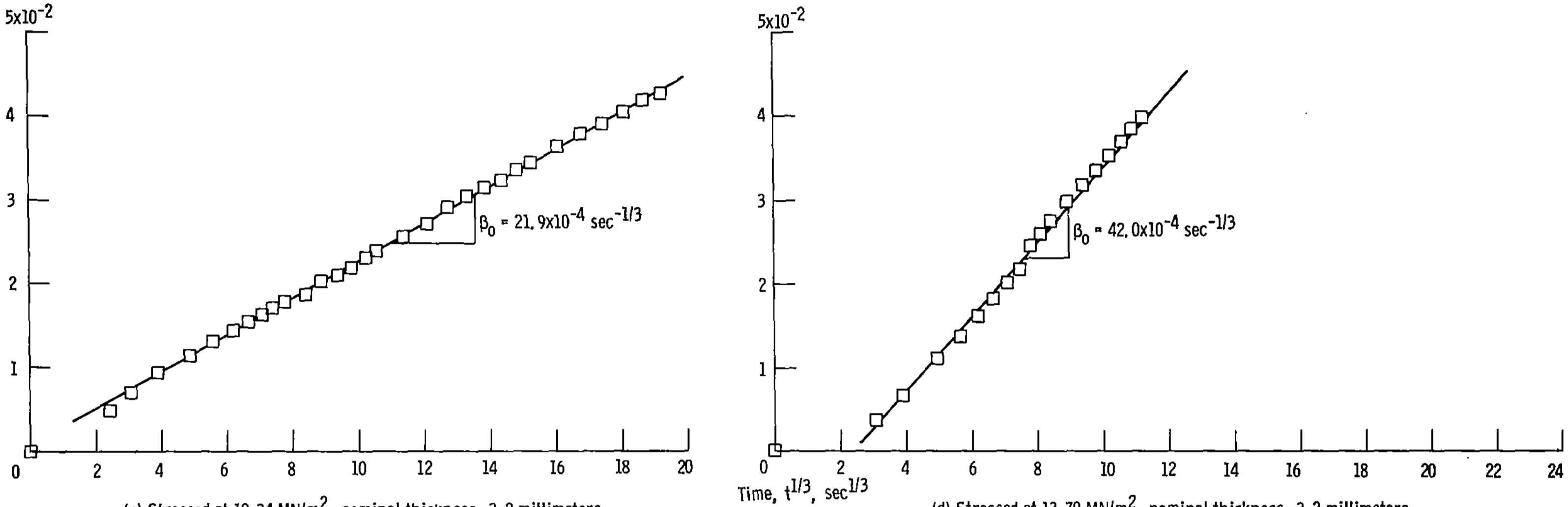

(c) Stressed at 10.34 MN/m^2; nominal thickness, 3.2 millimeters.

(d) Stressed at 13.79 MN/m^2; nominal thickness, 3.2 millimeters.

Figure 11. - Strain-time relations for deformation behavior of Nickel-201 in helium at 1000° C.

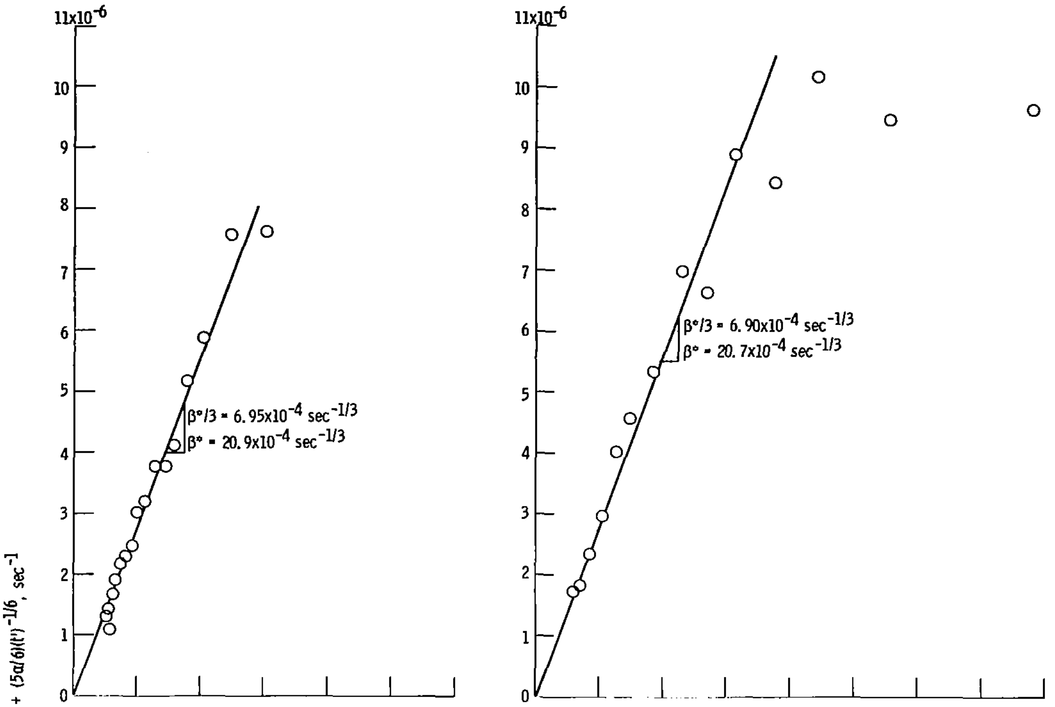

(a) Stressed at 6.90 MN/m^2; nominal thickness, 3.2 millimeters; scale barrier coefficient, 0.48x10^{-5} second$^{-5/6}$.

(b) Stressed at 6.90 MN/m^2; nominal thickness, 1.6 millimeters; scale barrier coefficient, 0.60x10^{-5} second$^{-5/6}$.

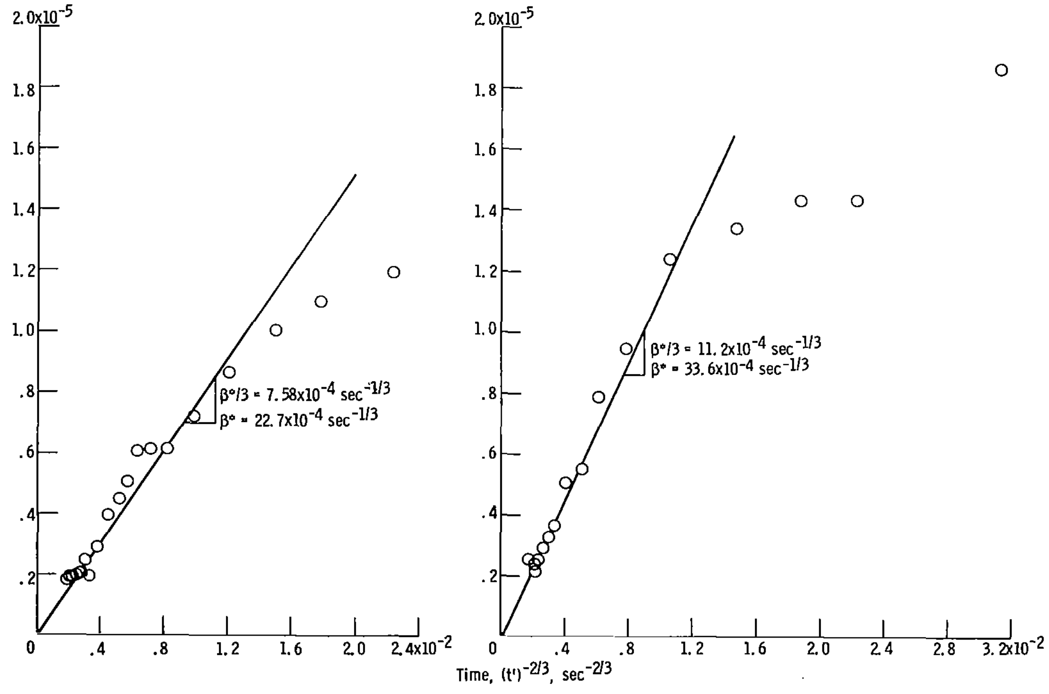

(c) Stressed at 10.34 MN/m^2; nominal thickness, 3.2 millimeters; scale barrier coefficient, 0.60x10^{-5} second$^{-5/6}$.

(d) Stressed at 13.79 MN/m^2; nominal thickness, 3.2 millimeters; scale barrier coefficient, 0.10x10^{-5} second$^{-5/6}$.

Figure 12. - Strain rate-time relations for deformation behavior of Nickel-201 tested in oxygen at 1000° C immediately subsequent to a deformation in helium at 1000° C.

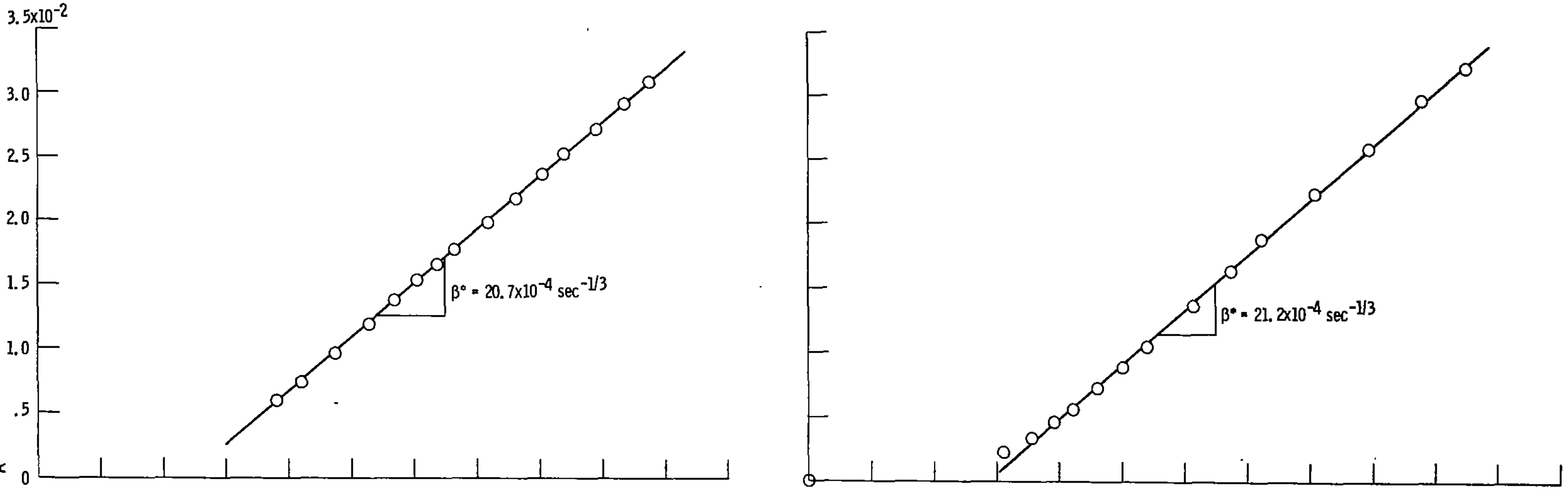

(a) Stressed at 6.90 MN/m^2; nominal thickness, 3.2 millimeters; scale barrier coefficient, 0.48x10^{-5} second$^{-5/6}$.

(b) Stressed at 6.90 MN/m^2; nominal thickness, 1.6 millimeters; scale barrier coefficient, 0.60x10^{-5} second$^{-5/6}$.

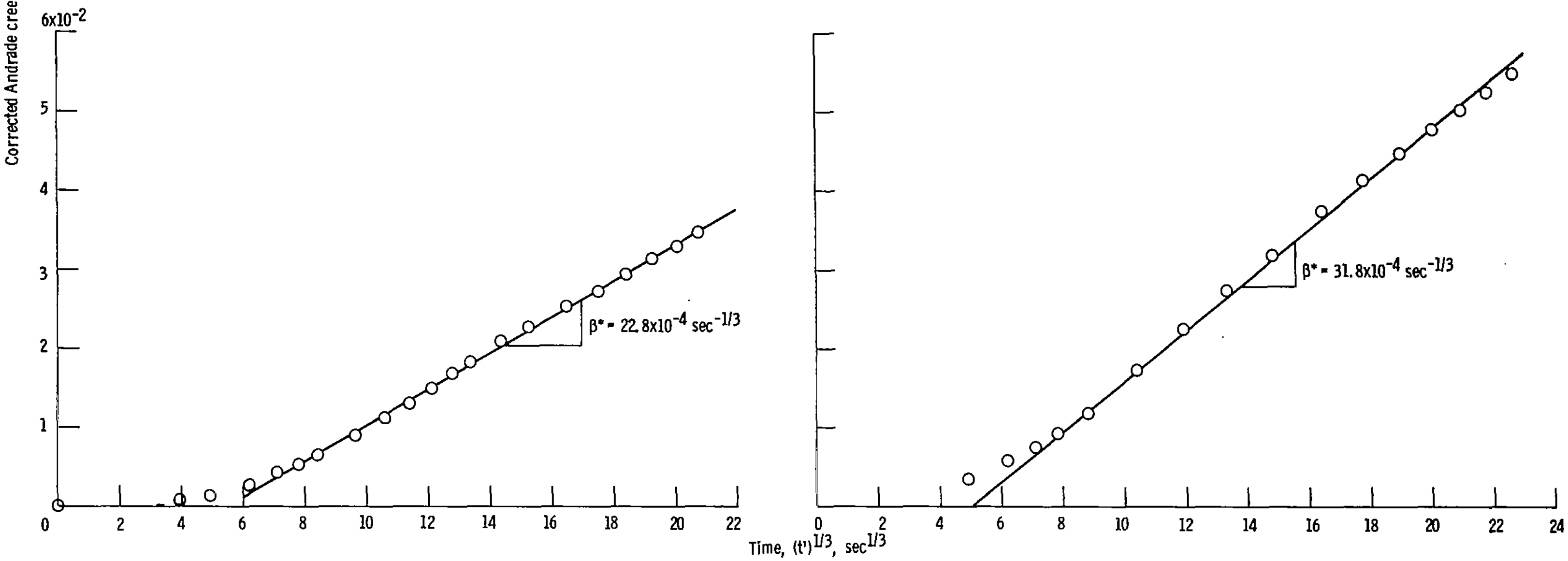

(c) Stressed at 10.34 MN/m^2; nominal thickness, 3.2 millimeters; scale barrier coefficient, 0.60x10^{-5} second$^{-5/6}$.

(d) Stressed at 13.79 MN/m^2; nominal thickness, 3.2 millimeters; scale barrier coefficient, 0.10x10^{-5} second$^{-5/6}$.

Figure 13. - Strain-time relations for deformation behavior of Nickel-201 in oxygen at 1000° C immediately subsequent to deformation in helium at 1000° C.

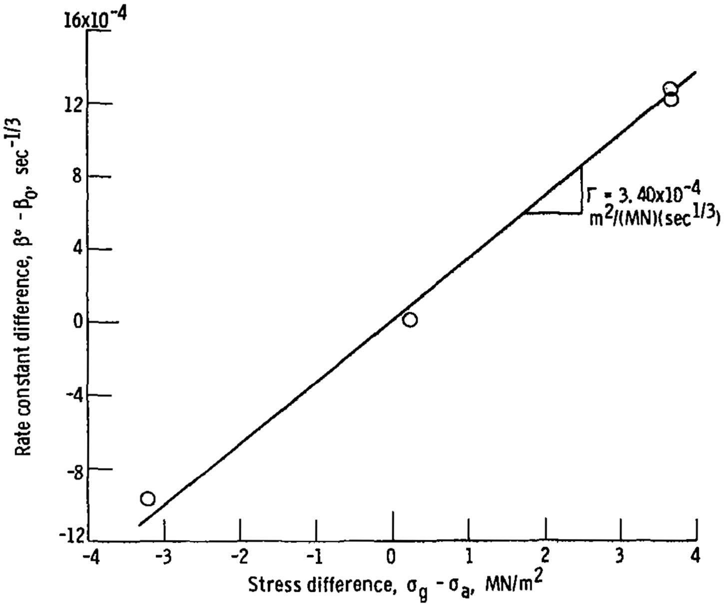

Figure 14. - Graphical interpretation of equation (20) illustrating proportionality of stress differences and creep rate differences for Nickel-201 specimens tested at 1000° C and for assumed grain boundary pressure σ_g of 10.59 MN/m^2.

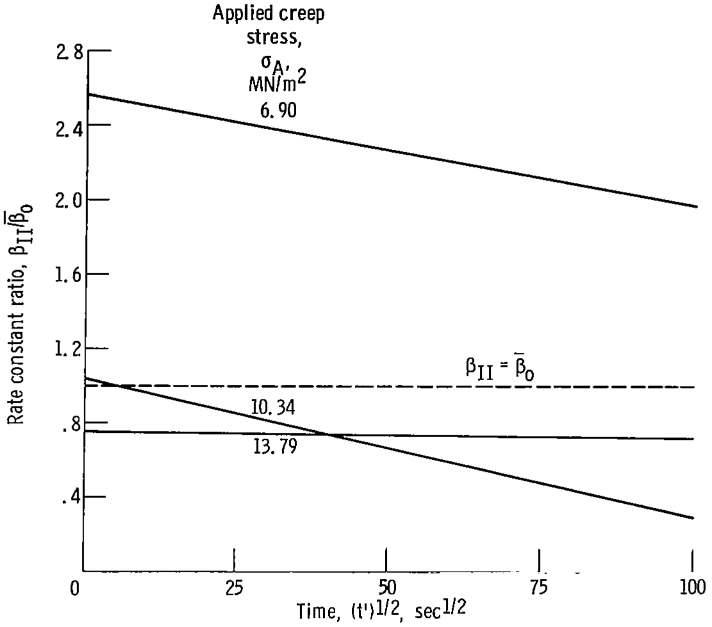

Figure 15. - Time dependence of ratio of effective Andrade creep rate constant in oxygen to that in helium at three levels of applied stress for Nickel-201 specimens tested at 1000° C. Ratios greater than unity imply that deformation rates in oxygen are greater than those in helium.

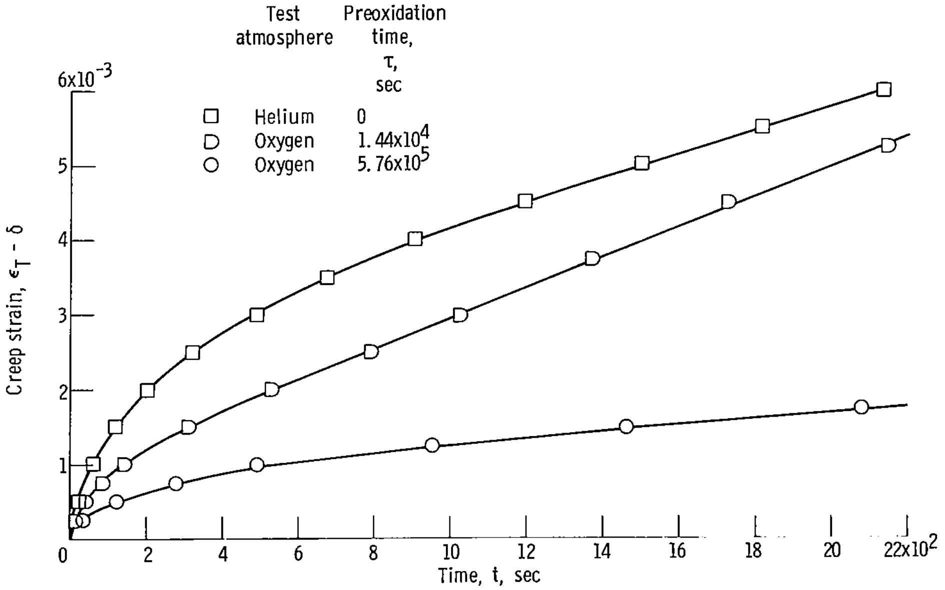

Figure 16. - Deformation behavior of Nickel-201 at 1000° C in helium and oxygen atmospheres and under applied stress of 6.90 MN/m^2. Nominal specimen thickness, 3.2 millimeters.

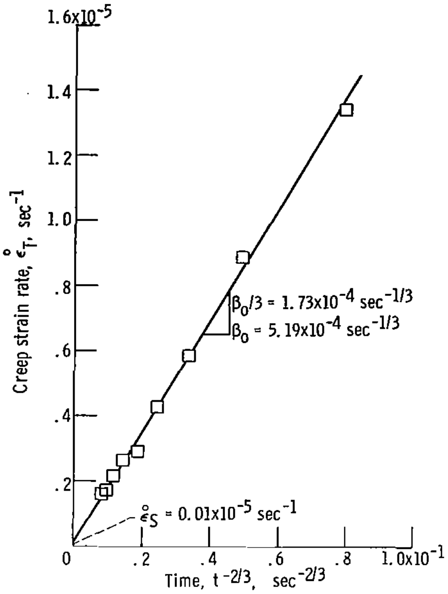

(a) Tested in helium.

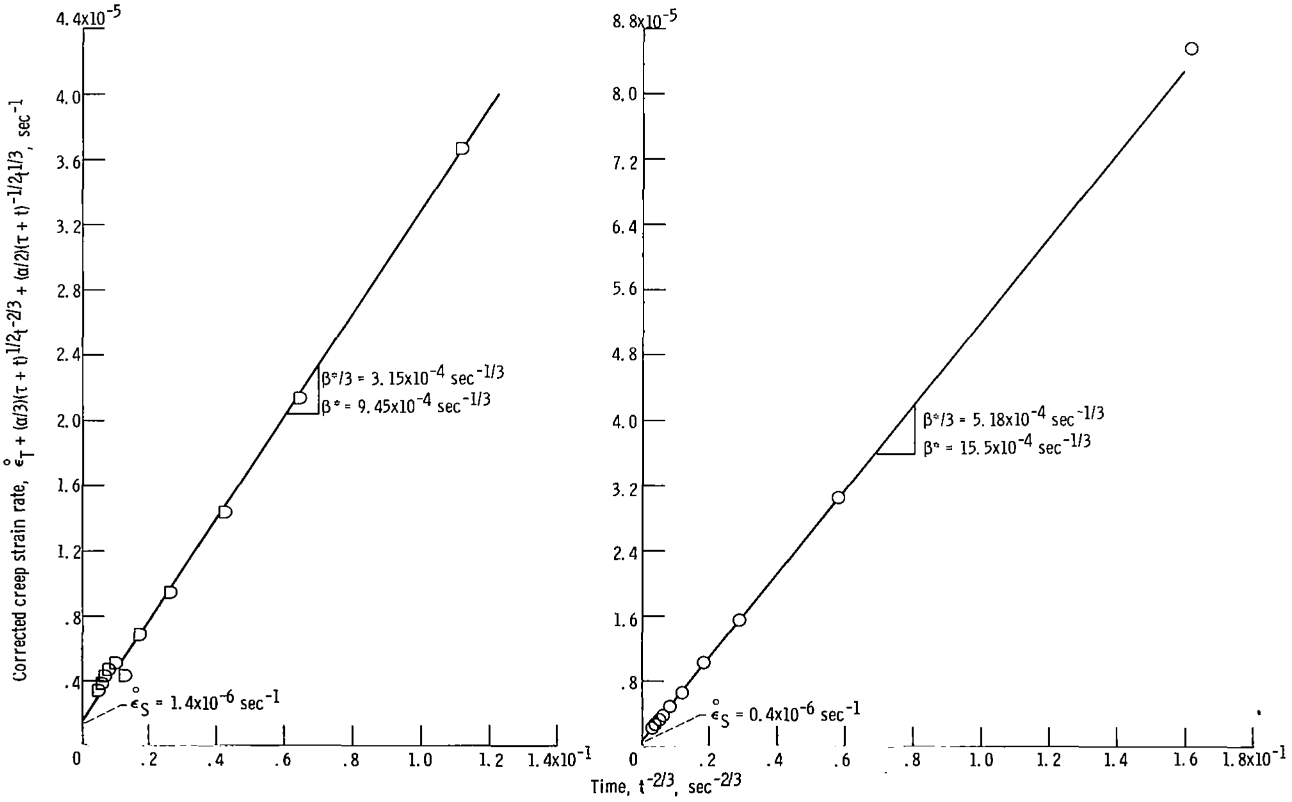

(b) Tested in oxygen after 1.44x10^4 seconds preoxidation.

(c) Tested in oxygen after 5.76x10^4 seconds preoxidation.

Figure 17. - Strain rate-time relations for deformation of 3.2-millimeter-thick specimens of Nickel-201 tested at 1000° C under applied stress of 6.90 MN/m^2.

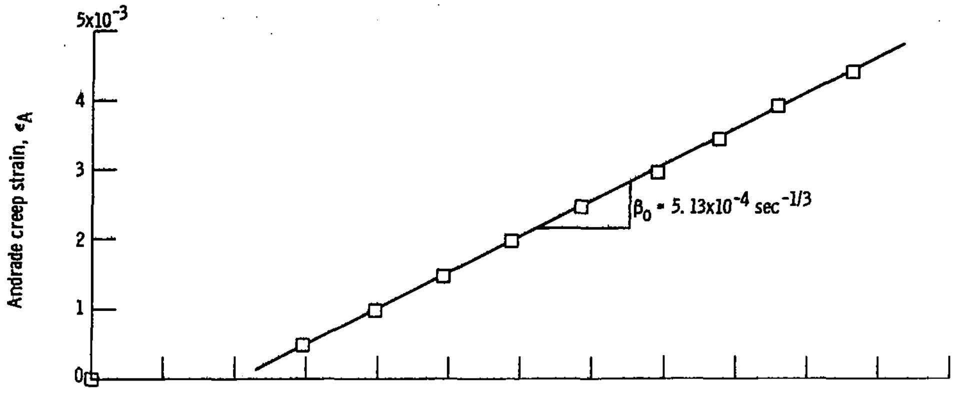

(a) Tested in helium.

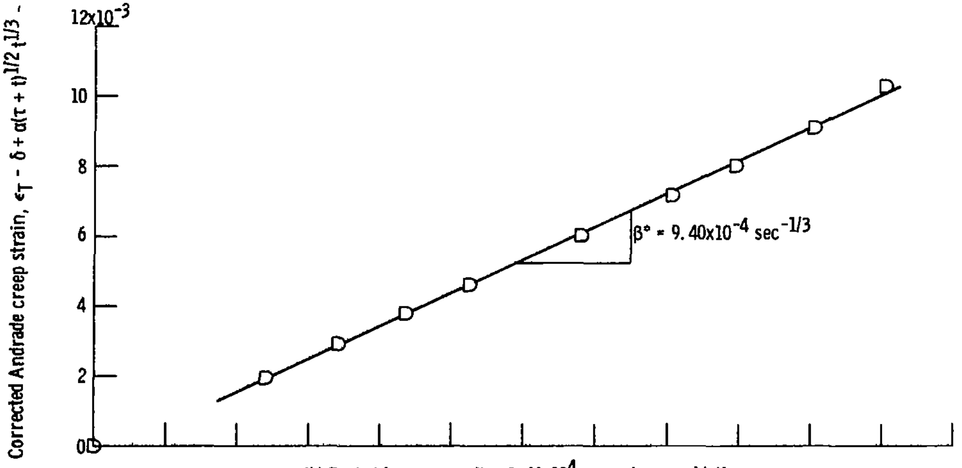

(b) Tested in oxygen after 1.44×10^4 seconds preoxidation.

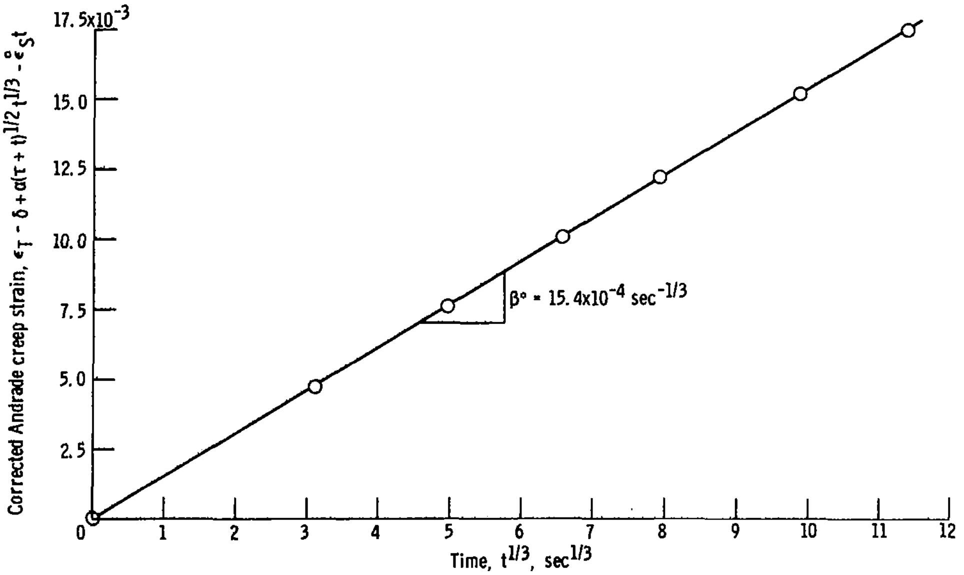

(c) Tested in oxygen after 5.76×10^4 seconds preoxidation.

Figure 18. - Strain-time relations for deformation of 3.2-millimeter-thick specimens of Nickel-201 tested at 1000° C under applied stress of 6.90 MN/m^2.

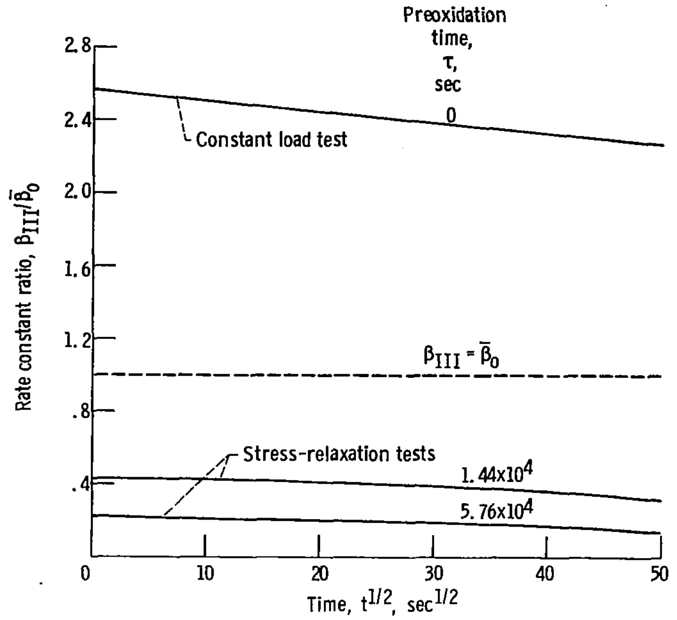

Figure 19. - Time dependence of ratio of effective Andrade creep rate constant in oxygen to that in helium for Nickel-201 specimens stressed to 6.90 MN/m^2 at 1000° C.

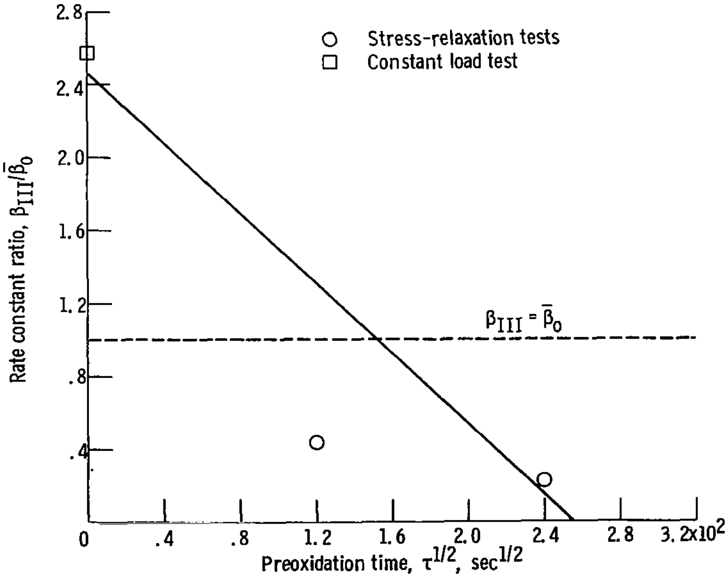

Figure 20. - Dependence of ratio of effective Andrade creep rate constant in oxygen to that in helium upon preoxidation time for Nickel-201 specimens stressed to 6.90 MN/m^2 at 1000° C.

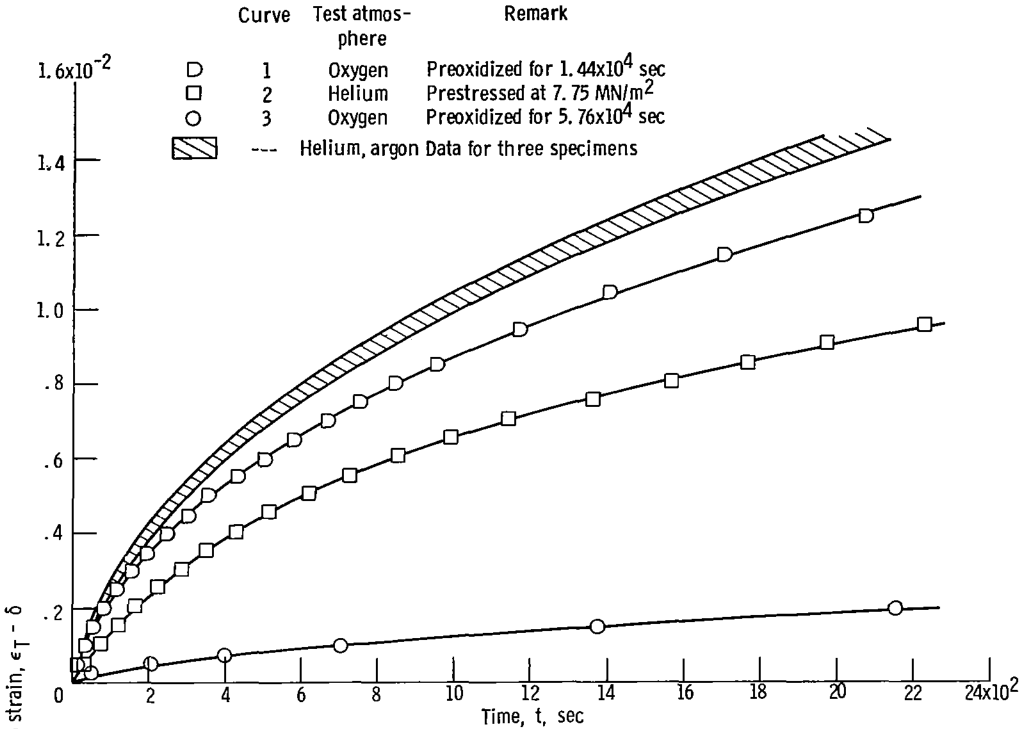

(a) Stressed at 6.90 MN/m^2 in helium and oxygen.

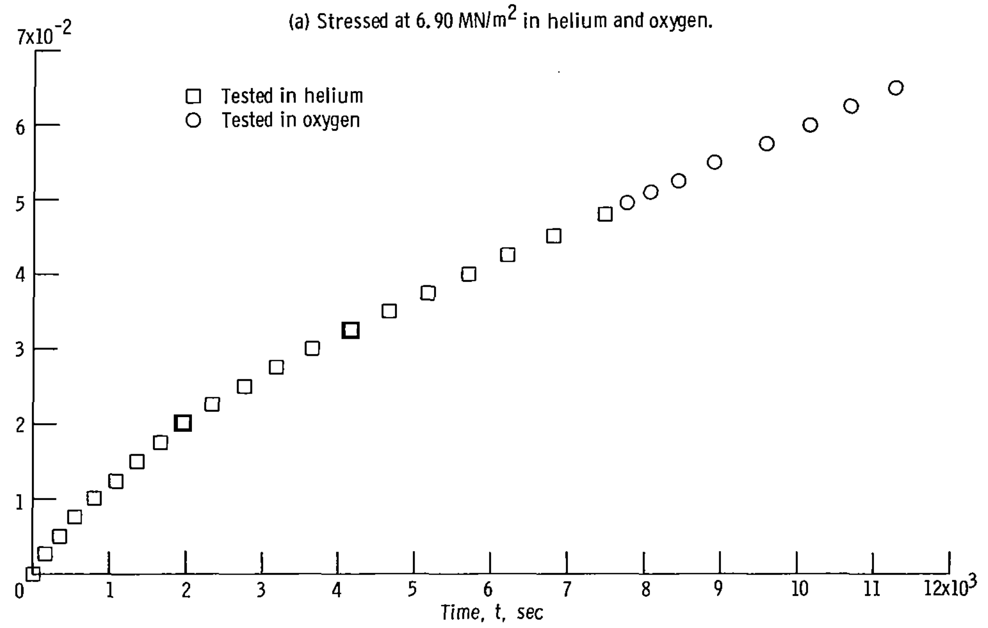

(b) Stressed at 10.34 MN/m^2 in helium, then in oxygen.

Figure 21. - Deformation behavior of Nickel-270 at 1000° C. Nominal thickness, 3.2 millimeters.

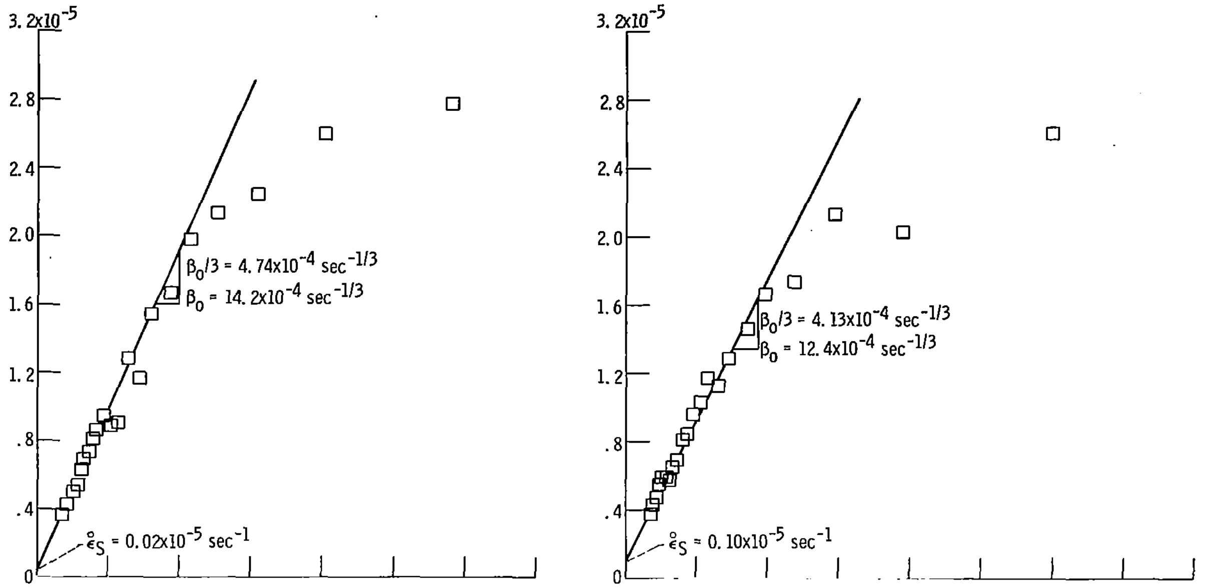

(a) Helium atmosphere; 6.90 MN/m^2.

(b) Argon atmosphere; 6.90 MN/m^2 (test 1).

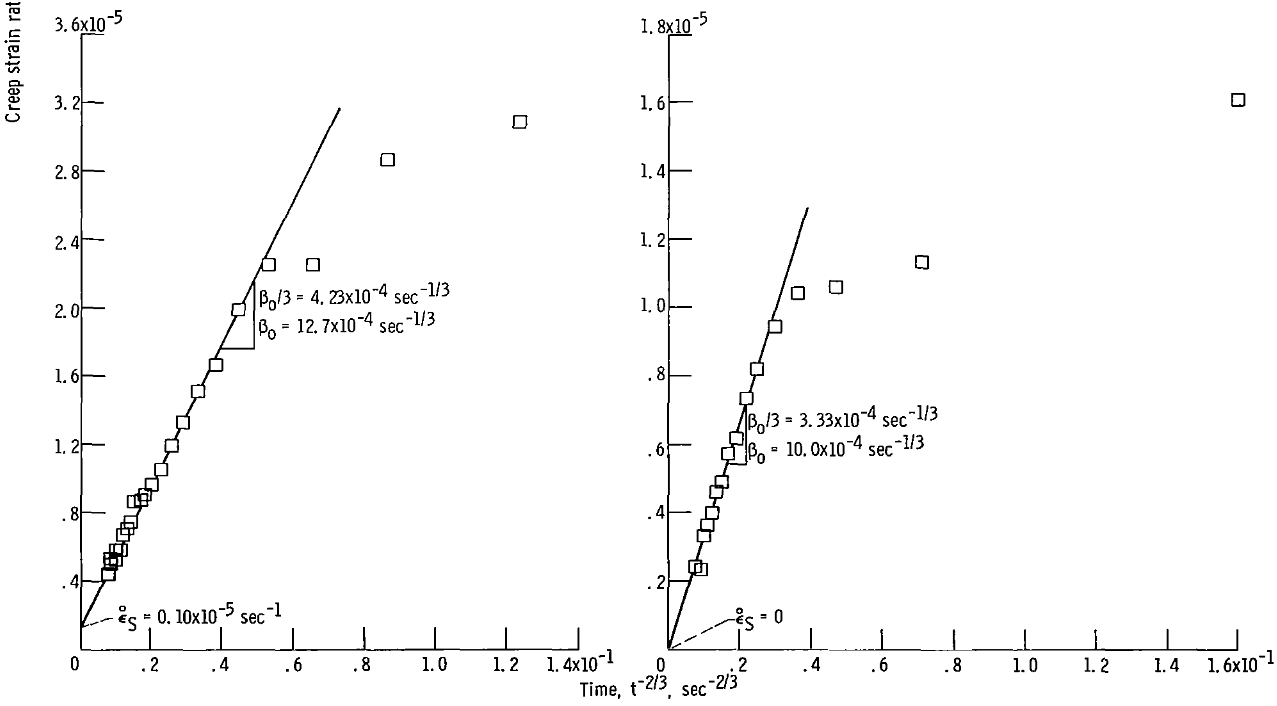

(c) Argon atmosphere; 6.90 MN/m^2 (test 2).

(d) Helium atmosphere; 6.90 MN/m^2 (7.75 MN/m^2 prestress).

Figure 22. - Strain rate-time relations for deformation of 3.2-millimeter-thick specimens of Nickel-270 tested at 1000° C.

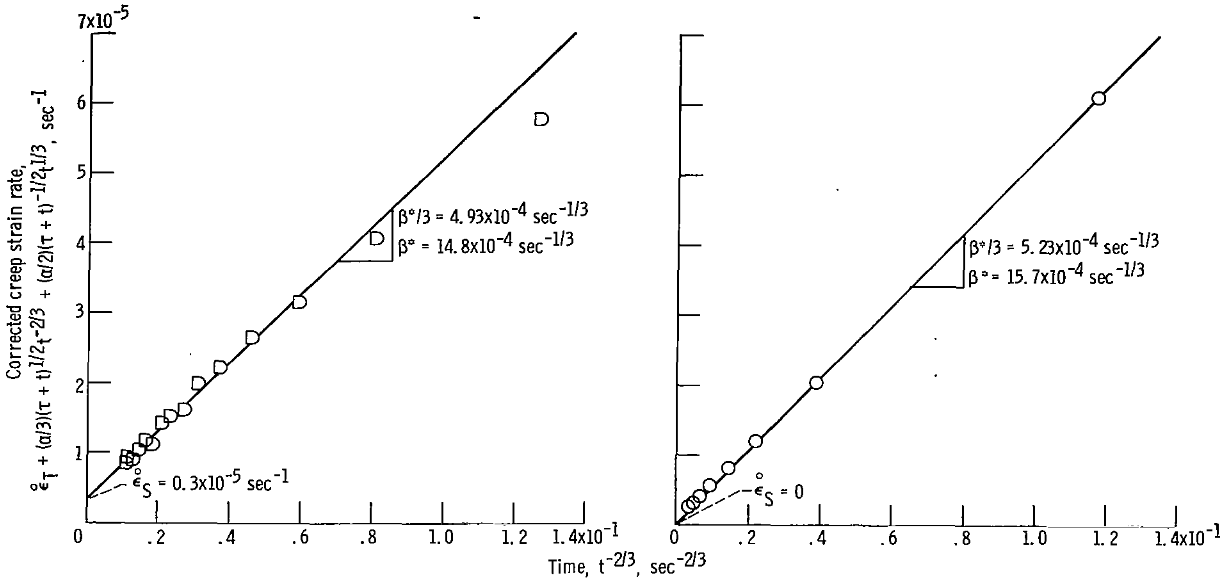

(e) Oxygen atmosphere; 6.90 MN/m²; 1.44x10⁴ seconds preoxidation; scale barrier coefficient, 0.60x10⁻⁵ second⁻⁵/⁶.

(f) Oxygen atmosphere; 6.90 MN/m²; 5.76x10⁴ seconds preoxidation; scale barrier coefficient, 0.60x10⁻⁵ second⁻⁵/⁶.

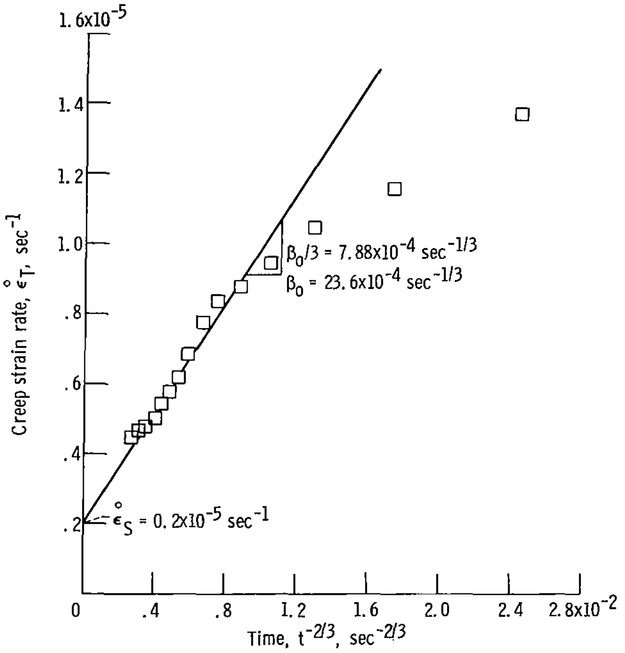

(g) Helium atmosphere; 10.34 MN/m².

Figure 22. - Concluded.

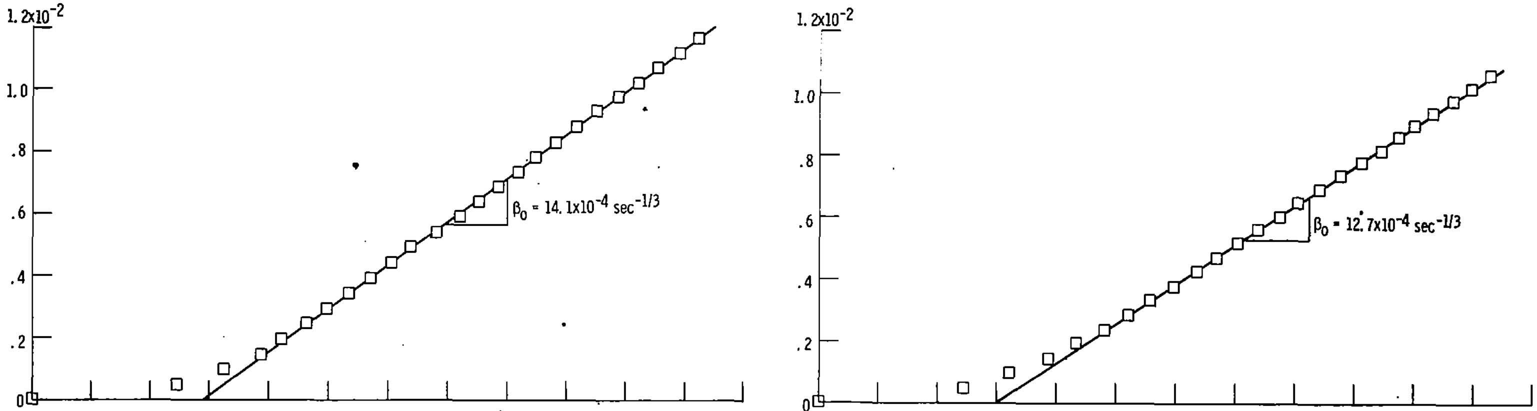

(a) Helium atmosphere; 6.90 MN/m^2.

(b) Argon atmosphere; 6.90 MN/m^2 (test 1).

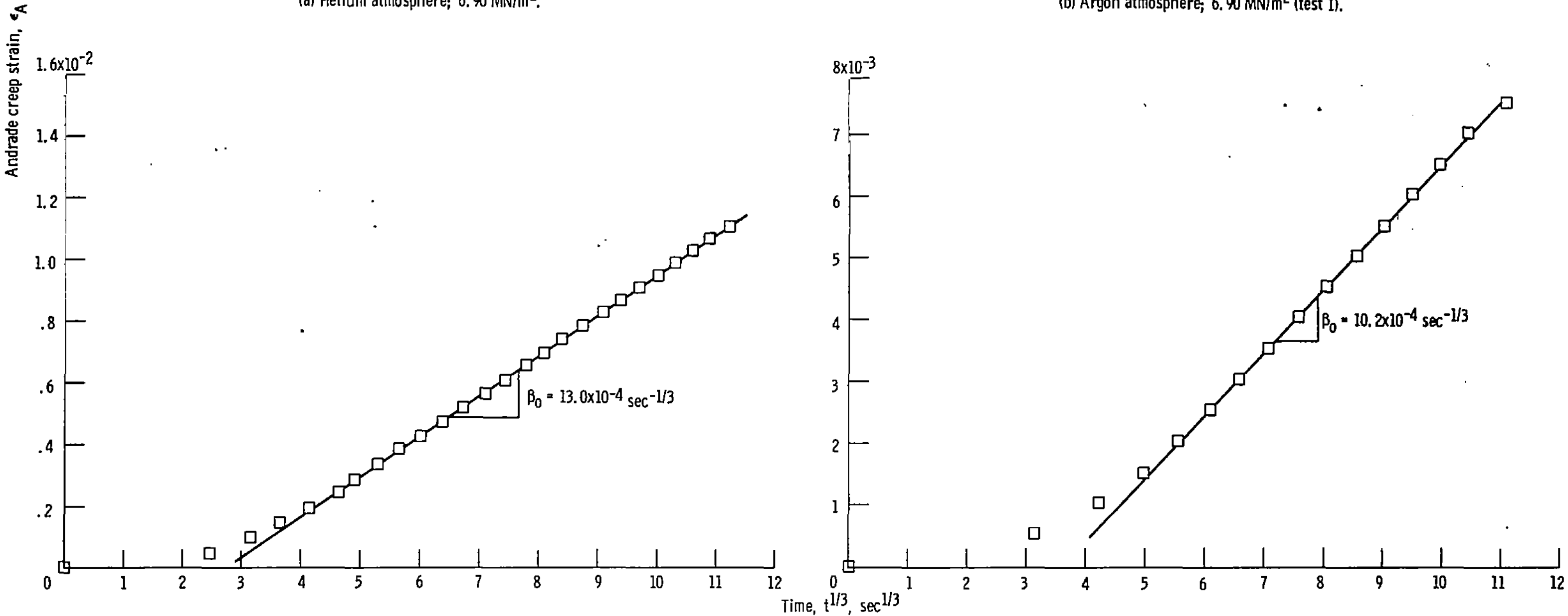

(c) Argon atmosphere; 6.90 MN/m^2 (test 2).

(d) Helium atmosphere; 6.90 MN/m^2 (7.75 MN/m^2 prestress).

Figure 23. - Strain-time relations for deformation of 3.2-millimeter-thick specimens of Nickel-270 tested at 1000° C.

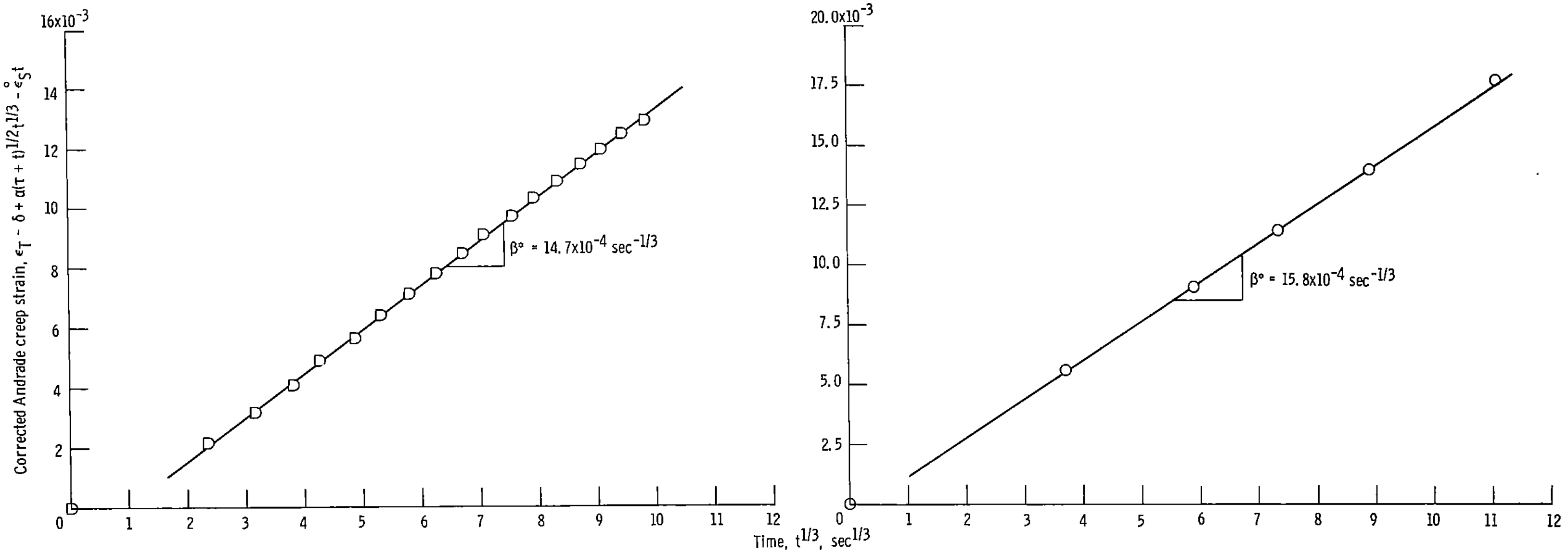

(e) Oxygen atmosphere; 6.90 MN/m^2; 1.44x10^4 seconds preoxidation; scale barrier coefficient, 0.60x10^{-5} second$^{-5/6}$.

(f) Oxygen atmosphere; 6.90 MN/m^2; 5.76x10^4 seconds preoxidation; scale barrier coefficient, 0.60x10^{-5} second$^{-5/6}$.

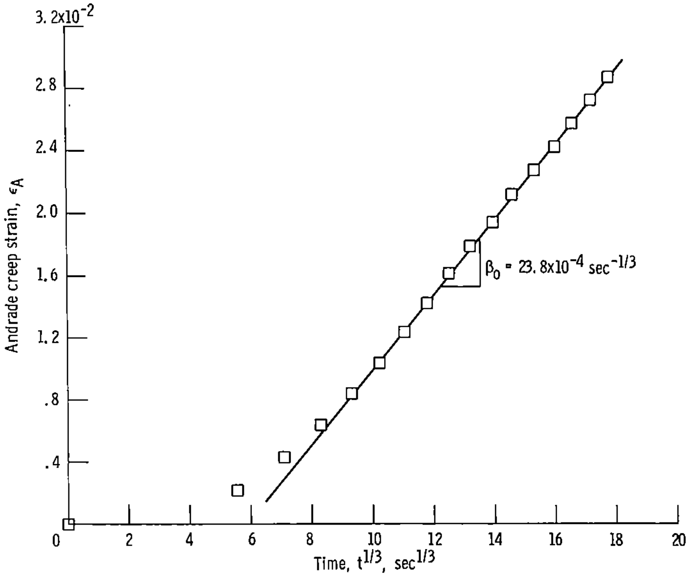

(g) Helium atmosphere; 10.34 MN/m^2.

Figure 23. - Concluded.

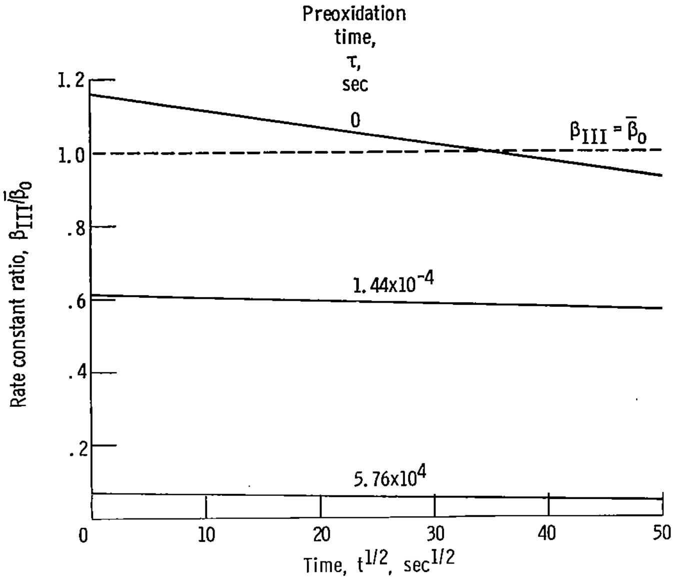

Figure 24. - Time dependence of ratio of effective Andrade creep rate constant in oxygen to that in helium for Nickel-270 specimens stressed to 6.90 MN/m^2 at 1000° C.

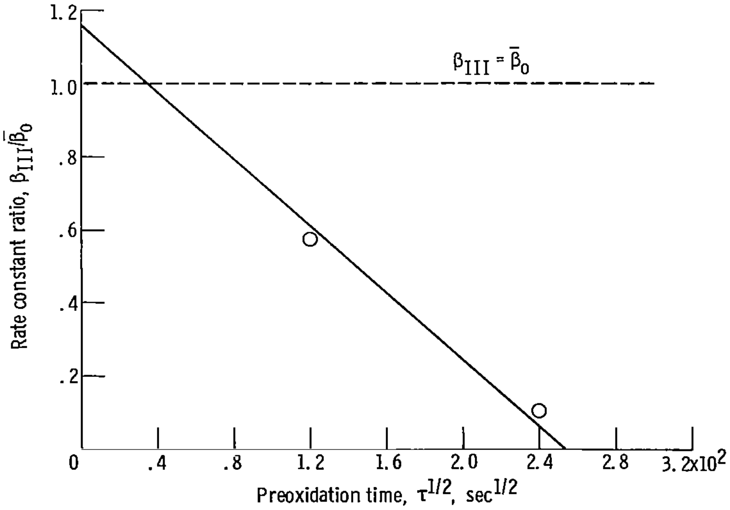

Figure 25. - Dependence of ratio of effective Andrade creep rate constant in oxygen to that in helium upon preoxidation time for Nickel-270 specimens stressed to 6.90 MN/m^2 at 1000° C.

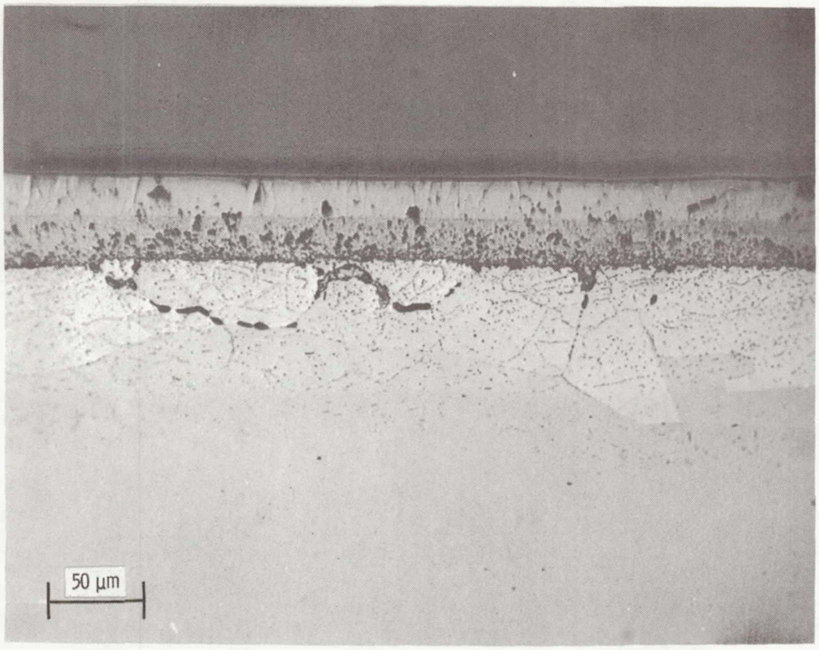

(a) Nickel-201 oxidized for 6.51x10^4 seconds.

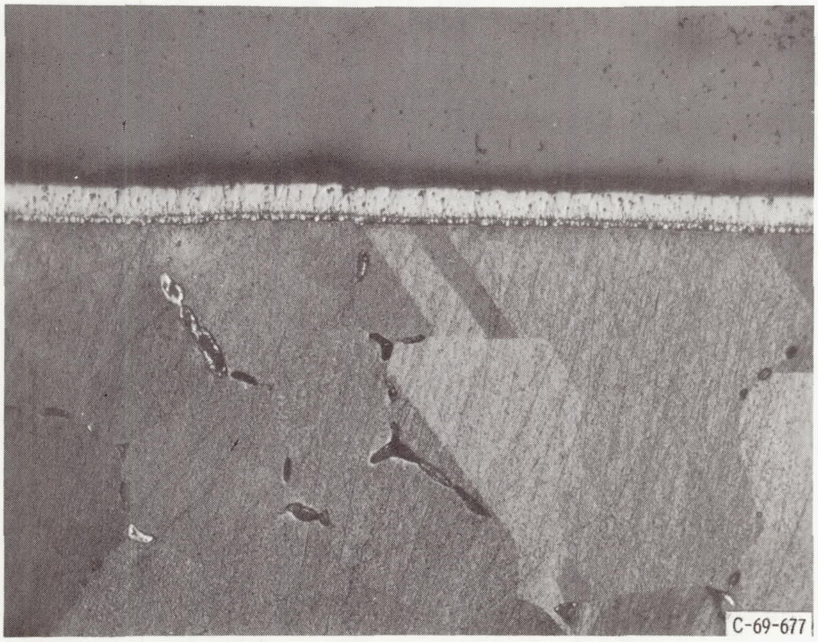

(b) Nickel-270 oxidized for 6.46x10^4 seconds.

Figure 26. - Photomicrographs showing reaction products in cross section for undeformed specimens of nickel oxidized at 1000° C. X250.

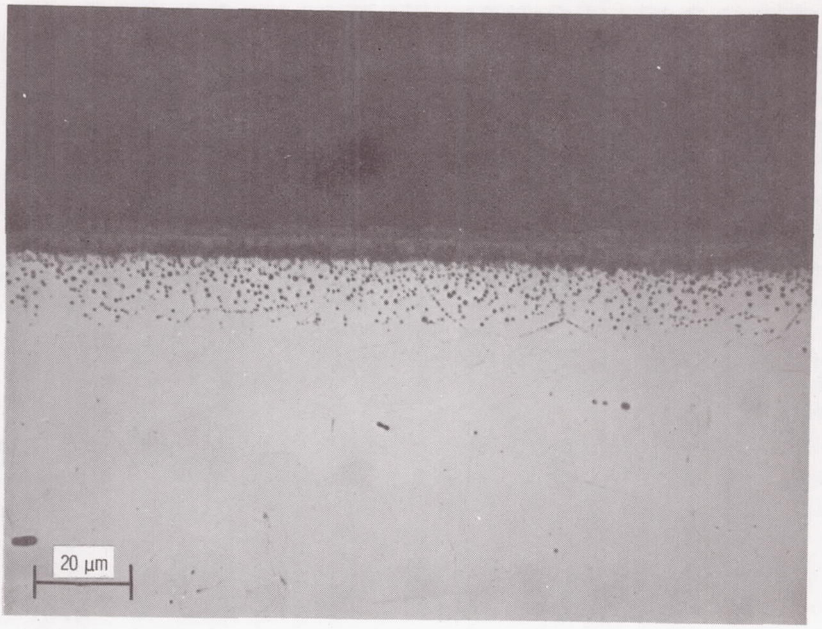

(a) Unstressed control specimen.

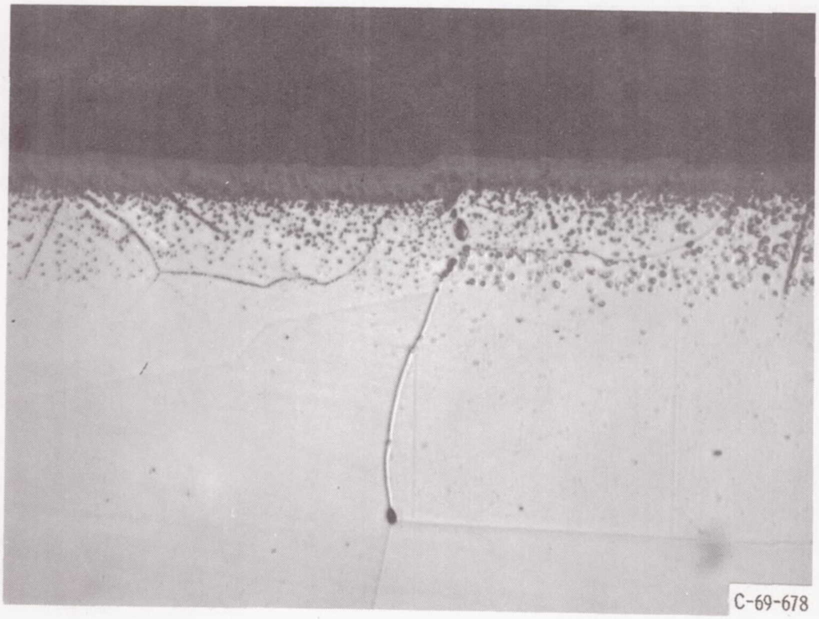

(b) Specimen stressed to 6.90 MN/m^2.

Figure 27. - Photomicrographs illustrating structure in cross section of stressed and unstressed specimens of Nickel-201 oxidized at 1000° C for 1.98×10^4 seconds. X500.

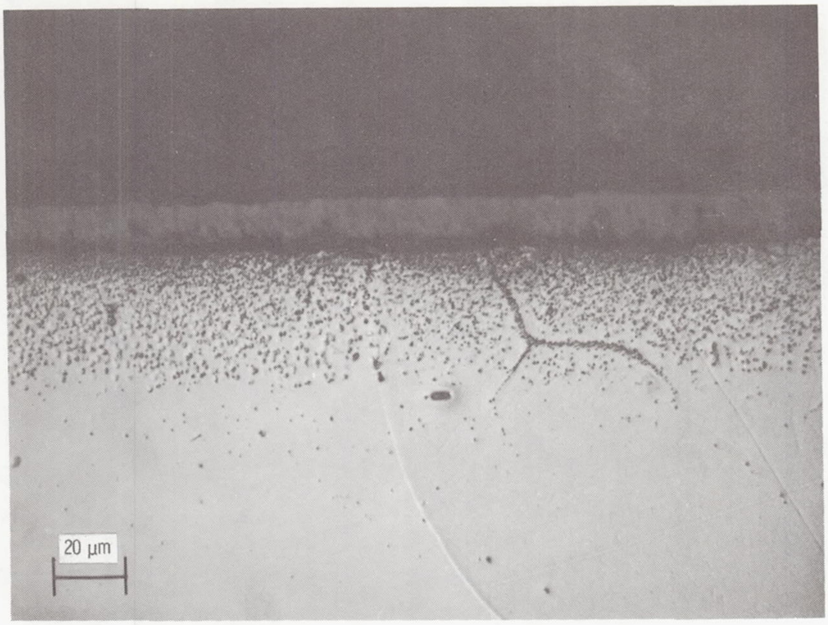

(a) Unstressed control specimen.

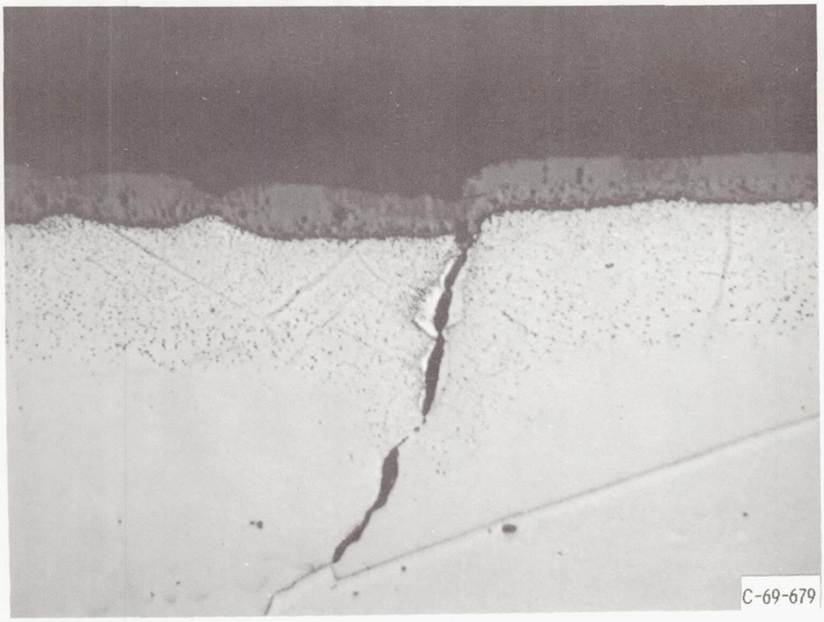

(b) Specimen stressed to 13.79 MN/m^2.

Figure 28. - Photomicrographs illustrating structure in cross section of stressed and unstressed specimens of Nickel-201 oxidized at 1000° C for 1.46×10^4 seconds. X500.

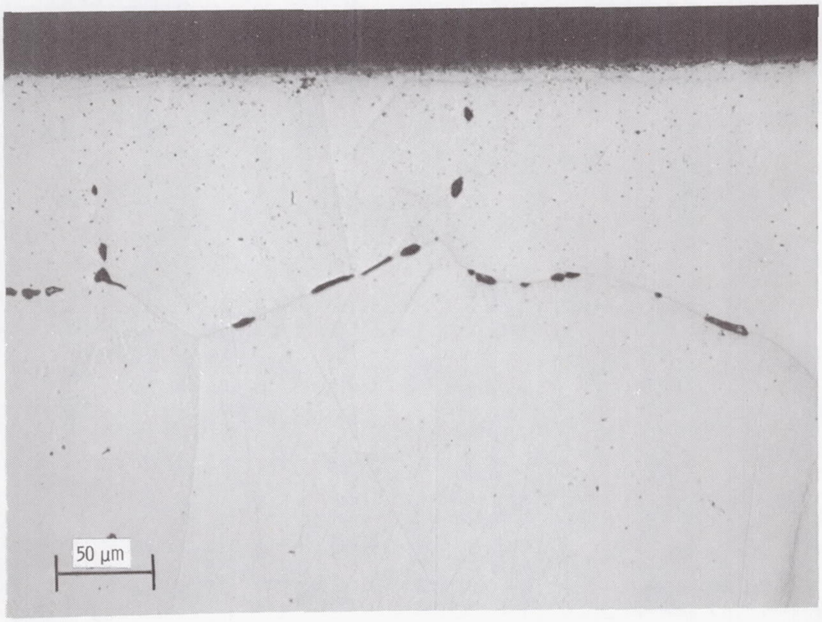

(a) Unstressed control specimen.

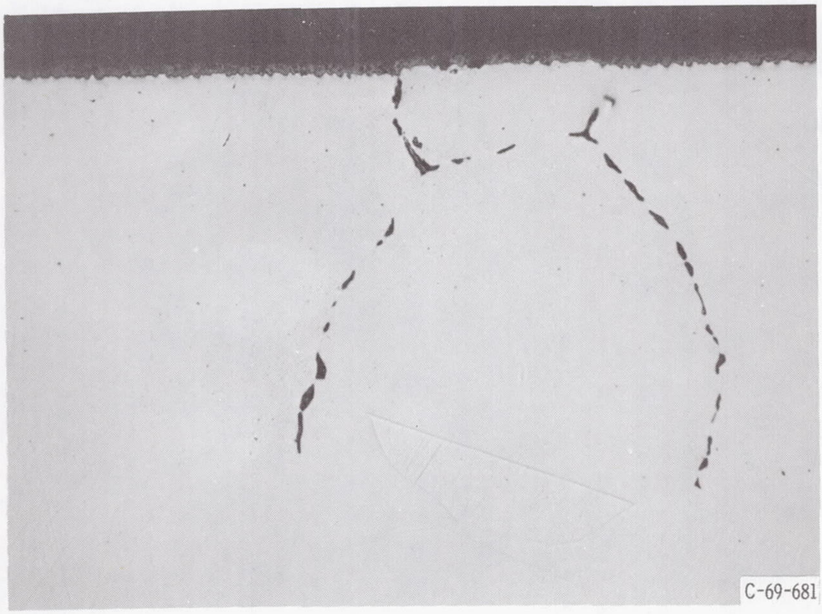

(b) Specimen stressed to 6.90 MN/m^2.

Figure 30. - Photomicrographs illustrating structure in cross section of stressed and unstressed specimens of Nickel-270 oxidized at 1000° C for 1.08×10^4 seconds. X250.

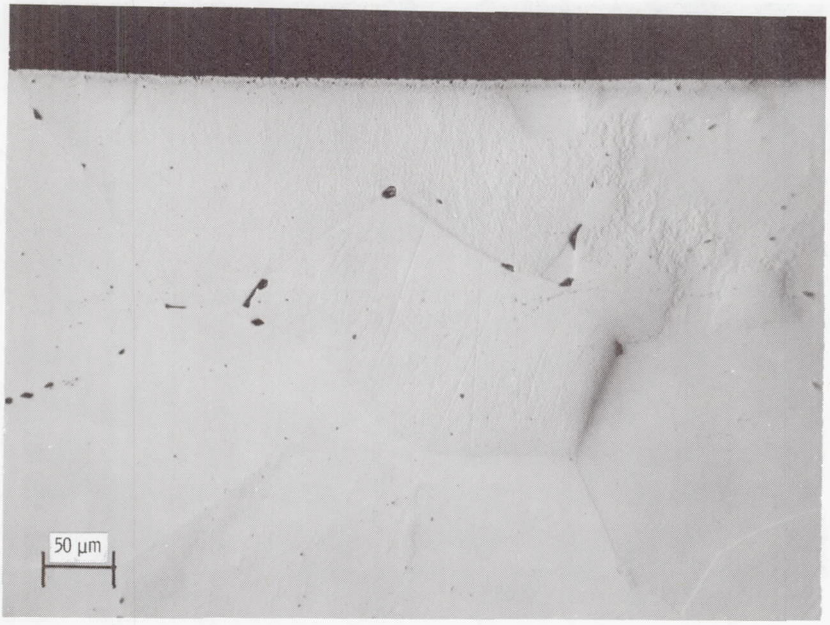

(a) Unstressed control specimen.

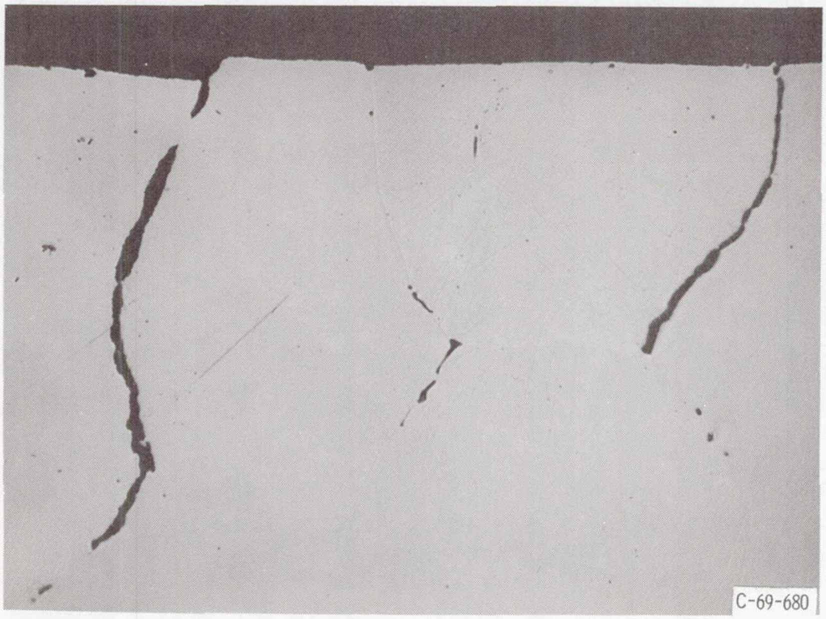

(b) Specimen stressed to 10.34 MN/m^2.

Figure 29. - Photomicrographs illustrating structure in cross section of stressed and unstressed specimens of Nickel-270 oxidized at 1000° C for 0.44×10^4 seconds. X250.

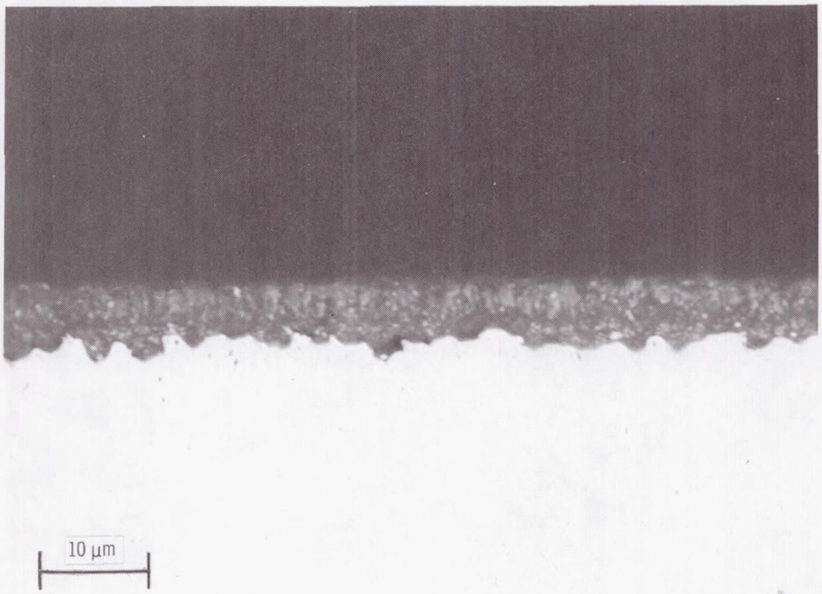

(a) Unstressed control specimen.

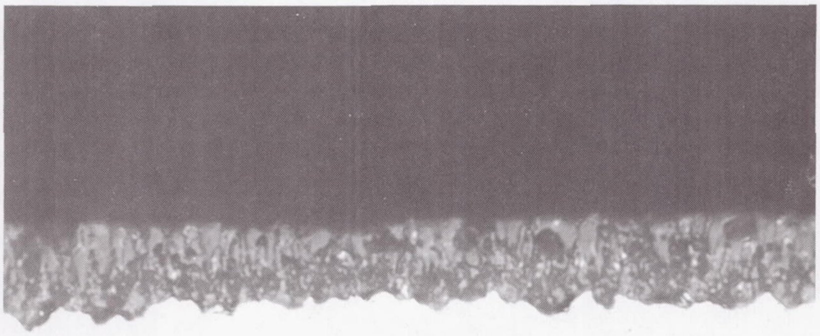

C-69-682

(b) Specimen stressed to 6.90 MN/m^2.

Figure 31. - Photomicrographs illustrating external scale structure in cross section for stressed and unstressed specimens of Nickel-270 oxidized at 1000° C for $1.08x10^4$ seconds. X1500.